QEX

September/October 2020

www.arrl.org

A Forum for Communications Experimenters

Issue No. 322

KZ1W and N7QT operate their 160 m – 17 m vertical antenna among palm trees.

APRS® / D-STAR®

TH-D74A 144/220/430 MHz Tribander

The TH-D74A represents the ultimate in APRS and D-STAR performance. KENWOOD has already garnered an enviable reputation with the TH-D72A handheld APRS amateur radio transceiver. Now it has raised the bar even further with the TH-D74A, adding support for D-STAR, the digital voice & data protocol developed by the JARL, and enabling simultaneous APRS and D-STAR operation – an industry first.

- APRS compliance using packet communication to exchange real-time GPS position information and messages
- Compliant with digital/voice mode D-STAR digital amateur radio networks
- Built-in high performance GPS unit with Auto Clock Setting
- Wide-band and multi-mode reception
- 1.74" (240 x 180 pixel) Transflective color TFT display
- IF Filtering for improved SSB/CW/AM reception
- High performance DSP-based audio processing & voice recording
- Compliant with Bluetooth, microSD & Micro-USB standards
- External Decode function (PC Decode 12kHz IF Output, BW:15 kHz)
- Free software for Memory and Frequency Control Program
- Data Import / Export (Digital Repeater List, Call sign, Memory Channel)
- Four TX Power selections (5/2/0.5/0.05 W)
- Dust and Water resistant IP54/55 standards

APRS (The Automatic Packet Reporting System) is a registered American trademark of WB4APR (Mr. Bob Bruninga).
D-Star is a digital radio protocol developed by JARL (Japan Amateur Radio League).

KENWOOD

Customer Support/Distribution Customer Support:
(310) 639-4200 Fax: (310) 537-8235

www.kenwood.com/usa

ISO9001 Registered

ADS#38619

QEX (ISSN: 0886-8093) is published bimonthly in January, March, May, July, September, and November by the American Radio Relay League, 225 Main St., Newington, CT 06111-1400. Periodicals postage paid at Hartford, CT and at additional mailing offices.

POSTMASTER: Send address changes to: QEX, 225 Main St., Newington, CT 06111-1400
Issue No. 322

Publisher
American Radio Relay League

Kazimierz "Kai" Siwiak, KE4PT
Editor

Lori Weinberg, KB1EIB
Assistant Editor

Scotty Cowling, WA2DFI
Ray Mack, W5IFS
Contributing Editors

Production Department

Becky R. Schoenfeld, W1BXY
Publications Manager

Michelle Bloom, WB1ENT
Production Supervisor

David Pingree, N1NAS
Senior Technical Illustrator

Brian Washing
Technical Illustrator

Advertising Information

Janet L. Rocco, W1JLR
Business Services
860-594-0203 – Direct
800-243-7768 – ARRL
860-594-4285 – Fax

Circulation Department

Cathy Stepina
QEX Circulation

Offices

225 Main St., Newington, CT 06111-1400 USA
Telephone: 860-594-0200
Fax: 860-594-0259 (24-hour direct line)
Email: **qex@arrl.org**

Subscription rate for 6 print issues:

In the US: $29

US by First Class Mail: $40;

International and Canada by Airmail: $35

ARRL members receive the digital edition of *QEX* as a member benefit.

In order to ensure prompt delivery, we ask that you periodically check the address information on your mailing label. If you find any inaccuracies, please contact the Circulation Department immediately. Thank you for your assistance.

About the Cover

Grant Saviers, KZ1W, and Robert Fanfant, N7QT, operated as H4ØTT during their November, 2019 "suitcase" DXpedition on Pigeon Island. Their 17 m to 160 m vertical antenna had a net height of 55 feet of fiberglass poles, around which was wound a continuously loaded spiral helix of 151 feet of wire. The antenna was capacitively top loaded to improve radiation efficiency. The four loading wires also doubled as part of the top level of guy wires. All of the antenna components were transported as checked luggage without difficulty from Seattle through Lomlom, and return. Travel from the Lomlom coral airstrip to Pigeon Island included wading through a lagoon, followed by a boat ride through mangrove swamps. The DXpedition yielded nearly 14,000 contacts in 11 days. [Grant Saviers, KZ1W, photo.]

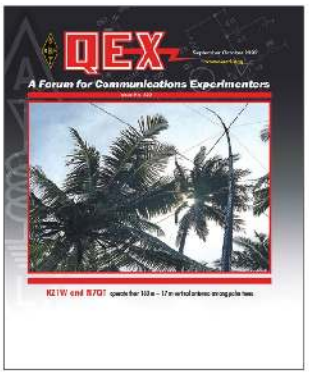

In This Issue

Index of Advertisers

The American Radio Relay League

The American Radio Relay League, Inc, is a noncommercial association of radio amateurs, organized for the promotion of interest in Amateur Radio communication and experimentation, for the establishment of networks to provide communications in the event of disasters or other emergencies, for the advancement of the radio art and of the public welfare, for the representation of the radio amateur in legislative matters, and for the maintenance of fraternalism and a high standard of conduct.

ARRL is an incorporated association without capital stock chartered under the laws of the state of Connecticut, and is an exempt organization under Section 501(c)(3) of the Internal Revenue Code of 1986. Its affairs are governed by a Board of Directors, whose voting members are elected every three years by the general membership. The officers are elected or appointed by the Directors. The League is noncommercial, and no one who could gain financially from the shaping of its affairs is eligible for membership on its Board.

"Of, by, and for the radio amateur," ARRL numbers within its ranks the vast majority of active amateurs in the nation and has a proud history of achievement as the standard-bearer in amateur affairs.

A *bona fide* interest in Amateur Radio is the only essential qualification of membership; an Amateur Radio license is not a prerequisite, although full voting membership is granted only to licensed amateurs in the US.

Membership inquiries and general correspondence should be addressed to the administrative headquarters:

ARRL
225 Main St.
Newington, CT 06111 USA
Telephone: 860-594-0200
FAX: 860-594-0259 (24-hour direct line)

Officers

President: Rick Roderick, K5UR
P.O. Box 1463, Little Rock, AR 72203

The purpose of *QEX* is to:

1) provide a medium for the exchange of ideas and information among Amateur Radio experimenters,

2) document advanced technical work in the Amateur Radio field, and

3) support efforts to advance the state of the Amateur Radio art.

All correspondence concerning *QEX* should be addressed to the American Radio Relay League, 225 Main St., Newington, CT 06111 USA. Envelopes containing manuscripts and letters for publication in *QEX* should be marked Editor, *QEX*.

Both theoretical and practical technical articles are welcomed. Manuscripts should be submitted in word-processor format, if possible. We can redraw any figures as long as their content is clear. Photos should be glossy, color or black-and-white prints of at least the size they are to appear in *QEX* or high-resolution digital images (300 dots per inch or higher at the printed size). Further information for authors can be found on the Web at **www.arrl.org/qex/** or by e-mail to **qex@arrl.org**.

Any opinions expressed in *QEX* are those of the authors, not necessarily those of the Editor or the League. While we strive to ensure all material is technically correct, authors are expected to defend their own assertions. Products mentioned are included for your information only; no endorsement is implied. Readers are cautioned to verify the availability of products before sending money to vendors.

Kazimierz "Kai" Siwiak, KE4PT

Perspectives

Like a Science Fiction Movie

Everything is going virtual. A peek at *Upcoming Conferences* reveals that conferences are now going to be either virtual events or they are postponed. Major DXpeditions are also being cancelled or postponed. DXing has come to a near standstill. Our new lexicon features *social distancing*, *masks*, *lock-down* and *stay-at-home* — phrases with new meanings. Elbow bumps replace handshakes. Ham club meetings are increasingly held online or over ham FM repeaters. Even ARRL Field Day recognized the reality of stay-at-home mandates by introducing a few new temporary rules. The FCC recently affirmed and made it clear that nothing in the FCC's rules prohibits remote amateur radio license testing, and prior FCC approval is not required. So amateur radio exams are also being held remotely.

The camaraderie of face-to-face interaction in the workplace is giving way to just doing a job in isolation. How are you handling things as shut-ins? How is your amateur radio experience different under current conditions? What fun new things are you building or experimenting with?

These days we waken to an eerily different world, one where things are in a fog, unsettled and unnatural. "*Kind of like a science fiction movie, but it's real.*" — *Robert De Niro, actor.* Remember that this is also a good time for our members to catch up on and to enjoy the mental stimulation of *QEX*, *QST*, *On the Air* and *NCJ* online editions.

In This Issue

André Champel, F5SQ, alerts us in his Technical Note of a fire hazard in using window transmission line.

Gwyn Griffiths, G3ZIL; Rob Robinett, AI6VN, and Glenn Elmore, N6GN, estimate LF and HF Band noise while acquiring WSPR spots.

Carl Luetzelschwab, K9LA, comments in a Technical Note on extending the matching range of an 80 m antenna.

John Post, KA5GSQ, generates and receives SSB signals using GNU radio companion.

Grant Saviers, KZ1W, and Rob Fanfant, N7QT, report on their vertical antenna for the H4ØTT "suitcase" DXpedition to Pigeon Island.

Writing for *QEX*

Please keep the full-length *QEX* articles flowing in, or share a **Technical Note** of several hundred words in length plus a figure or two. *QEX* is edited by Kazimierz "Kai" Siwiak, KE4PT, (**ksiwiak@arrl.org**) and is published bimonthly. *QEX* is a forum for the free exchange of ideas among communications experimenters. All ARRL members can enjoy the *QEX* Online edition as a member benefit. The *printed edition* annual subscription rate (6 issues per year) for members and non-members is $29 in the United States. First Class mail delivery in the US is available at an annual rate of $40. For international subscribers, including those in Canada and Mexico, *QEX* printed edition can be delivered by airmail for $35 annually, see **www.arrl.org/qex**.

Would you like to write for *QEX*? We pay $50 per published page for full articles and *QEX* Technical Notes. Get more information and an Author Guide at **www.arrl.org/qex-author-guide**. If you prefer postal mail, send a business-size self-addressed, stamped (US postage) envelope to: *QEX* Author Guide, c/o Maty Weinberg, ARRL, 225 Main St., Newington, CT 06111.

Very kindest regards,
Kazimierz "Kai" Siwiak, KE4PT
QEX Editor

Grant Saviers, KZ1W

8730 250th Ave. NE, Redmond, WA 98053 USA;
kz1w@arrl.net

Robert Fanfant, N7QT

21422 NE 79th St., Redmond, WA 98053 USA;
rfanfant@hotmail.com

The H4ØTT "Suitcase" Vertical Antennas for 160 m to 17 m Bands

A report on the antennas and DXpedition operation on Pigeon Island.

We operated as H4ØTT on Lomlom/Pigeon Island (Reef Islands) during our November, 2019 "suitcase" DXpedition. The station was located on Pigeon Island, roughly 11 acres in size and surrounded by sea water. Our plan was to use vertical antennas on the beach (VOB) as our transmit antennas for simultaneous two-band operation. One vertical could operate from 10 m to 80 m, and the other from 17 m to 160 m.

Because of baggage limitations, the maximum size of the 160 m vertical antenna that we could transport and erect by the two of us, with some resident assistance, was the 18 m tall Spiderbeam (**www.spiderbeam.us**) telescopic fiberglass pole, which was 5 feet 7 inches when collapsed. Our net height was 55 feet excluding one of the top section poles, which was too flexible to be used. We capacitively top loaded the 160 m vertical to improve radiation efficiency. The four loading wires would also work as part of the top level of guy wires. We used a ski bag, though "curious" for a tropical location, to transport our fiberglass poles. They were transported as checked luggage without difficulty from Seattle to Los Angeles to Brisbane to Honiara to Lomlom, and return. Travel from the Lomlom coral airstrip to Pigeon Island included wading through a lagoon, followed by a boat ride through mangrove swamps.

Figure 1 — The vertical radiator spiral-wound inductor windings are spaced 1.4 inches. We got local help to construct and erect the antenna.

The Vertical Radiator

Inductors large enough to load the antenna to resonance would be problematic for mounting and maintaining on the tapered pole, and would be sensitive to salt air degradation at high power. We developed a spiral wound (helix) vertical using #16AWG insulated wire. Conveniently, *EZNEC/Pro4* has a feature to automatically generate a helix antenna with arbitrary length, start, and end diameters. With the four 21-foot long #16AWG insulated wires as top loading, it took a number of trials to obtain resonance over perfect ground at 1820 kHz. We selected guy anchor points to be at a 42-foot base radius to limit the footprint. This set the top loading wires at a 37° angle to the pole.

EZNEC allows a choice of the number of segments per spiral turn, as well as routing at the start and stop of the turns. This feature enabled us to model including the radial and top loading wires. The final model had more than 2,700 segments. The turn-to-turn voltage at high power was well under 100 V, so there was no concern about arcing from salt accumulation with insulated wire. Wire diameter, insulation thickness and performance were important to include in the model. There was no *EZNEC* method found to estimate the influence of the fiberglass pole properties on the antenna resonant point or efficiency. However, the

Figure 2 — The actual winding of wire onto the pole was from a 3-inch diameter cardboard mailing tube pre-wound with 151 feet of wire.

wound pole resonated as modeled. The fiberglass tube wall thickness varies from 0.07 inch to 0.03 inch from the 3 inch diameter bottom to the top, and appears to have a high glass to epoxy ratio.

We computed the length of wire to be 151 feet from the number of turns and the average diameter of the modeled constant taper per foot. This led to the calculation of the distance between turns based on the average diameter. The actual pole is not of uniform taper, so it took some tweaking to get the turn spacing even for the actual winding, which was about 1.4 inches, see **Figure 1**. Uneven spacing did not seem to affect the actual resonant point, and we concluded that wire length was more the controlling factor than even turn spacing given the large spacing of the turns.

The actual winding of wire onto the pole was from a 3-inch diameter cardboard mailing tube pre-wound with 151 feet of wire, **Figure 2**. We found passing the pre-wound tube back and forth under the fully extended pole with one of us on each side was the fastest and least fatiguing winding method.

We fabricated a short length of aluminum rod in KZ1W's machine shop for the top of the pole. We made five tapped 10-32 holes to attach the end of the spiral vertical wire to the 4 top loading wires. The coax feed point choke was 23 turns of RG400 coax on a 4-inch #31 ferrite core, Fair-Rite 2631814002.

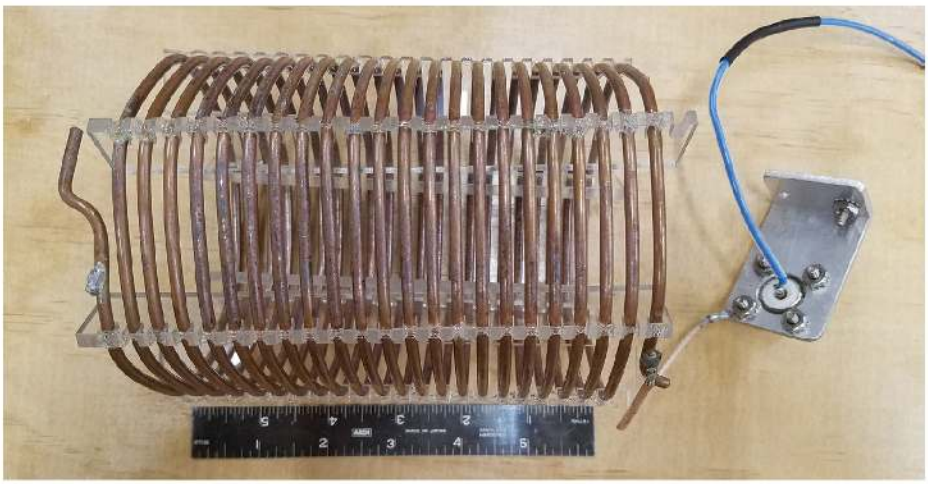

Figure 3 — The radial loading coil design uses six 1/8" thick by 1/2" deep acrylic coil supports.

Figure 4 — One of the CrankIR adjustable elevated radial assemblies is shown flanked by authors KZ1W and N7QT.

Coil Loaded Elevated Radials

Radial design is another challenge for a limited space 160 m vertical. Our prior VOB experience was very successful with two elevated quarter-wave radials. However two 133-foot elevated radials end to end was longer than any distance available to us on Pigeon Island. Modeling by Rudy Severns, N6LF, **[1]** predicted very little performance degradation for short inductively loaded radials when placed above sea water. We expected to be less than a quarter wavelength away from the tide line and based on prior modeling **[2]** by one of us (KZ1W) indicates this to be a reasonable guide. Modeling showed a single 22 µH of loading inductance permitted radials to be shortened to 72 feet. We built several prototype coils using different wire sizes and coil form materials to characterize the needed inductance of 22 µH and Q above 300 to reduce the loss in the coils. We tried skeletonized 3-inch PVC pipes, several 3D printed ABS and PLA forms, various wire sizes, as well as a commercial coil, but none exceeded a Q of 200.

The final coil design (**Figure 3**) used six 1/8-inch thick by 1/2-inch deep acrylic coil supports. The wire slots for the #8AWG solid copper wire were gang-milled in 6 acrylic supports at two times the wire diameter pitch, which is the recommended pitch for high-Q coils. For a winding form, a 3.5-inch diameter UHMW (Ultra High Molecular Weight) solid bar was slotted in both a 4 and 6 pattern for holding the acrylic supports, which were temporarily held in place with tape. The wire was wound by hand into the slots by turning the lathe chuck, then an acrylic solvent-based adhesive was applied to the entire length of each support over the wire in the slots. The adhesive does not stick to UHMW plastic. After allowing 24 hours to cure, the finished coil was then carefully slid off the UHMW mandrel with the acrylic supports intact. We measured a Q close to 300 using a vector network analyzer. Predictions were twice

that value. See the N3OX reference **[3]** for improved Q measurement techniques.

The coil design was rugged enough to survive the round trip to H4ØTT and almost two weeks of use outdoors. We made a rain cover for the coil from a large diameter mailing tube thoroughly impregnated with acrylic spray. The covers eventually came apart in the frequent torrential rains, but did not affect the antenna tuning. The next version of the cover will be a thermally formed acrylic sheet.

For radials we used SteppIR CrankIR radial assemblies that gave us great flexibility for ensuring the actual antenna on site resonated at 1820 kHz, and the ability to shift the resonant frequency a bit. SteppIR **[4]** graciously provided these and a vertical wire spool assembly as well (seen in **Figure 4**). All three had 150 feet of wire so the wound pole design as well as a backup **L** design could be implemented for the unknown site conditions, see more details in **Figure A** in the **www.arrl.org/qexfiles** web page.

The 160 m helix vertical antenna uses one coil to resonate the two shortened elevated radials, a helix-wound elevated radials, a helix-wound vertical section, and a top hat. It was built and erected in KZ1W's back yard. It easily resonated as modeled at 1820 kHz with 72-foot radials. With the two radials elevated 6.5 feet the resonant impedance was 28 Ω. The modeled impedance was 12 Ω at resonance, so ground and vertical losses made up the difference. Daylight comparison tests over a 2 mile path to N7QT from the KZ1W 160 m **T** antenna, an 85-foot high vertical with eight 125-foot long radials elevated 10 feet above ground, showed a 1 or 2 dB higher signal compared to the helix antenna. Nighttime comparison testing using FT8 mode by KZ1W over 750 and 1650 mile paths showed the helix design to be 3 to 4 dB down from his **T** antenna. This testing was difficult due to QSB, so heard report *vs.* sent report normalization was the basis for the estimates. The difference in the modeled gain over average ground of the two antennas had the helix short radial antenna 2.6 dB below the KZ1W reference **T** antenna.

Just before departing for the DXpedition, modeling showed that a wire run to the top of the pole and back down a bit would resonate on 80 m with the radials at a quarter wavelength using the CrankIR radial assembly, the radial coil shorted and no connection to the helix and top load wires. Four-foot long lateral spreaders at mid pole height and a CrankIR top spreader (about 36 inches) assembly spaced the wire both up and down from the coil. The vertical wire feeding spool from a CrankIR was used, see **Figure B** in **www.arrl.org/qexfiles**. Now we had both a helix 160 m vertical and a tall CrankIR for 80 m. Subsequently, on the island, we found that the CrankIR wire adjacent to the helix vertical would resonate up to 17 m, but above that there was too much interaction with the vertical and top hat wires. Effectively, we had a "super CrankIR" 160 m to 17 m antenna.

Further modeling after returning from the DXpedition showed that the vertical near sea water low angle pattern and gain were retained for higher bands. By using the *AutoEZ* optimizer, a 1.25:1 SWR match was found on 15 m. These dimensions are far from a quarter wavelength at 13-feet vertical with 7.5-foot radials. Thus, it is important to model each band and test the dimensions as these might be hard to find by trial and error. Once the approximate starting dimensions are known, the wide-range adjustment of the CrankIR makes tuning to a specific frequency an easy task.

Figure 5 — The 160 m vertical antenna was erected among the palm trees.

Installing the Antennas at H4ØTT

We had limited prior data about the island since *Google Earth* views were cloud covered and the island has an extensive palm tree canopy. We found a spot on the northwest side that had enough tree spacing to erect the antenna after some trimming of palm fronds (**Figure 5**). Unfortunately, every beach is several feet underwater at high tide. The only practical location was on

a cliff away from the tide line. Despite palm frond trimming, the fronds would contact the top load wires and antenna in heavy wind causing arcing and momentary spikes in our SWR.

After the expedition, we modeled the actual antenna location on island. As a reference, this antenna with short radials over sea water has a gain of 2 dBi at a few degrees of elevation. This is about 3.5 dB less than a full-size vertical with two elevated quarter wavelength radials. With this antenna located 75 feet from and 15 feet above the water with 72-foot radials, the gain towards the beach is 1 dBi at a few degrees and –2 dBi at 25° landward. Thus, the actual location on the northwest side of the island contributed to better propagation to Europe than to the USA.

At teardown we did find evidence of arcing from the top load, and the wound #16AWG 600 V rated wires due to contact with the palm tree foliage. Of course, the voltage is several thousand volts, but there was no place to site the 160 m antenna without some foliage contact. The HYE-QUE end insulators at the guy rope-to-wire junctions did their job, but high voltage wire was really required. Our prior experience at E51MKW with a high power 160 m CW station shows that arcing would have wiped out simultaneous operation on other bands.

Our second vertical used on 40 m through 15 m was located at the northeast tip of the island. It was a conventional CrankIR with a single radial, using a 30-foot MFJ telescopic fiberglass support pole. It was about 12 feet above the high tide line and 50 feet from the lagoon.

Reversible Receive Antennas

Two Double Half Delta Loops (DHDL), designed for the TX3A DXpedition, were used as the 160 m and 80 m receiving antennas. The dimensions were 25-feet high vertical wires and 66 feet between them. The DHDL directivity was reversible with remote relays activated by a bias **T** 12 V power injector located at the station on the RG6 feedline. One end of each DHDL was supported by a palm tree and the other was on a fiberglass pole. So we had four choices of receiver directivity. With the K3S receiver operating in diversity with DHDL and vertical antenna inputs for the two receivers, CW reception was dramatically improved.

H4ØTT Results

Propagation was poor on the upper bands. Compared to our previous South Pacific efforts, daytime bands opened late and closed early. The usual mid-day tropics propagation dead zone extended from 10:00 to 15:00 local time. At no time did we have 12 m or 10 m propagation. There were only a few short 15 m openings. The 20 m and 17 m bands were plagued with rapid QSB but were workable. Top band (160 m), 80 m, 40 m and 30 m were the best bands. We planned to operate two 1 kW stations.

On the second day, one amplifier would transmit at only 350 W and by day four it failed completely. With only one amplifier to swap between two operators and skewed sleeping times, we could not operate as much as we had hoped. Our daily QSO totals fell by 50% when the one amplifier failed.

We provisioned cell phones for data access and a Wi-Fi access point, but it turned out that we had no internet access. The thought of bringing a BGAN satellite terminal weighing over 10 pounds to allow near real-time logging was dropped early in the planning due to costs. Therefore, logs were not uploaded until we left the island.

We logged 13,980 QSOs in 11 days on the air, including the "bonus morning" when our weekly departing flight was cancelled. Operation on 160 m was a notable success with 899 QSOs. We lost a day to thunderstorms, and it took almost two full days to get the 160 m vertical and the DHDL antennas erected. Our verticals and DHDLs survived without damage in a windstorm that exceeded 40 knots. Prior to the operation we thought that the path to Europe was going to be the difficult, but found out it was much easier than working the east coast of North America. Europe garnered 25% of the total contacts compared with 28% to the USA.

Conclusions

We felt we proved the viability of a "suitcase" compact 160 m to 17 m vertical for future DXpeditions, particularly if it can be mounted as a true vertical on the beach. We learned that deploying a 160 m antenna and two DHDL receive antennas was very time consuming for a two person team. Our thinking is that for a suitcase DXpedition that includes 160 m, a larger team of 3 or 4 persons is desirable to share the workload, distribute the checked baggage weight as well as lowering the excess baggage fees (about $4,000 for us). A larger team would also permit bringing a third station for redundancy.

Grant Saviers, KZ1W, was first licensed KN3JEB circa 1958, then upgraded to General class. After receiving a BS and MS engineering degrees in 1968 he was inactive for a number of years. He became relicensed as Amateur Extra class in 1985, and operated as KZ1W for his offshore sailing and operation from two Massachusetts locations. Following a long career in computer storage systems at DEC, Adaptec, and several startups, he retired and moved to Redmond, WA where he built a mini-superstation and large machine shop. His DXpeditions include H4ØTT, TX5D, TX7G, and E51MKW.

Robert Fanfant, N7QT, graduated from U of WA and Washington State University with degrees in electrical engineering and material science. He worked at Intel manufacturing computer chips, then transitioned into software development. He retired in 2014 after a successful career at Applied Microsystem, Microsoft and software consulting. Rob obtained his Novice license (WN7TDU) at age 14, and upgraded to Amateur Extra class license in the mid 90s. His primary passion is combining a love of travel with chasing DX. In retirement he has given back to the amateur radio community by becoming the "DX" from H4ØTT, VK9MA, VK9WA, VP2MQT, TX5Z, TX5D, VK9AN, 5JØX, PJ7/N7QT, PJ6/N7QT, VP6D and V84SAA. His other passions include landscape photography, motorcycle adventure touring, gardening and spending time with family and friends.

References

[1] R. Severns, "Short Radials for Ground Plane Antennas," *ARRL Antenna Compendium Volume 6.*

[2] G. Saviers, "Verticals on the Beach – Some Modeling Results," *QST*, June 2016, pp. 32 – 34.

[3] **www.n3ox.net/tech/coilQ/.**

[4] **https://consumer.steppir.com/shop/accessories/crankir-option-adjustable-radial-unit-40m-2m/.**

Errata

In Steve Stearns, K6OIK, "General Uniform Transmission Lines: Power Efficiency, Loss, Standing Wave Ratio, and Return Loss," *QEX*, May/June 2020, the formula due to W. W. Macalpine in the third row second column of **Table 3** is missing a factor. The correct formula is

$$\frac{1}{\eta} = e^{2\alpha l}\,\frac{1-\left|\Gamma_{in}\right|^2-2\left|\Gamma_{in}\right|\left(\frac{X_0}{R_0}\right)\sin 2\psi_{in}}{1-\left|\Gamma_{L}\right|^2-2\left|\Gamma_{L}\right|\left(\frac{X_0}{R_0}\right)\sin 2\psi_{L}}$$

Regarding equations (18) and (23), "Riccati" is misspelled. Thanks to Luitjens Popken, of Leiden, NL, and Larry Bos, WØPSI, for noticing the error.

John E. Post, KA5GSQ
Embry-Riddle Aeronautical University, 3700 Willow Creek Road, Prescott, AZ 86301; **postj@erau.edu**

Generation and Reception of Single-sideband Signals using GNU Radio Companion

Apply digital signal processing techniques to generate and receive single-sideband signals using GNU Radio Companion software.

A Short History of Amateur Radio SSB

The year 2022 is the 75th anniversary of the first single-sideband radio telephony experiments conducted by the Stanford Radio Club on the 20 and 75 meter bands **[1]**. For over 50 years single-sideband suppressed carrier — also known as "SSB" and designated as J3E by the International Telecommunication Union — has been the dominant modulation for voice transmission in the amateur HF bands. Early on, two basic methods were recognized for generating single-sideband signals: 1) modulating a carrier with a baseband signal and then attenuating the undesired sideband with a filter — filter method — or 2) an arrangement of double modulators so that the carrier and modulating signal are phase shifted by 90° before being applied to the other modulator to permit cancellation of the undesired sideband — phasing method **[2]**. Either the filter method or the phasing method can also be applied to select the desired sideband at the receiving end.

Whether used in transmit or receive applications, both methods are complicated by the practical limitations of the hardware used to implement the circuits **[3]**. In the case of the filter method, arrangements of bulky mechanical, ceramic, or crystal filters are necessary to suppress the unwanted sideband at an intermediate frequency, followed by up-conversion to the desired transmit frequency. The primary limitation for the phasing method is the difficulty of generating exactly 90° of phase shift over the entire audio band **[4]**. Attempting to overcome the limitations of the filter and phase shift methods, Weaver **[5]** introduced a hybrid approach that is commonly referred to as Weaver's method, or the third method, for generation and reception of SSB signals.

Digital Signal Processing using *GNU Radio Companion*

Digital signal processing techniques provide several advantages for generating and receiving SSB signals compared with classic hardware-based techniques. Probably the most important is the ability to process signals using complex (in-phase and quadrature) representations instead of only real number representations. This greatly simplifies the task of sideband separation when generating and receiving SSB signals, as well as the task of frequency translation from carrier frequency to baseband, and vice-versa. The availability of digital processing blocks whose performance is almost indistinguishable from ideal components, particularly filters, is another compelling advantage. One limitation that must be considered follows from the Sampling Theorem: the bandwidth of real signals being processed must not exceed half of the sampling frequency, while the bandwidth of complex signals being processed must not exceed the sampling frequency itself.

GNU Radio Companion (*GRC*) is a free, open-source, Linux or PC-based software that contains the digital signal processing blocks necessary to implement software defined radio (SDR) functions **[6]**. A quick way of installing the PC-based version of *GRC* is to follow the workflow provided by the company that produces the SDR Play series of receivers **[7]**.This article will review the theoretical basis for the generation and reception of SSB signals and then present *GRC* flow graphs that implement those functions. The article concludes by presenting an example that applies *GRC* and a software defined radio to implement a full-duplex 70-cm SSB transceiver.

Filter Methods of SSB Generation

Two approaches are possible using the filter method: sideband selection at baseband before frequency translation to the carrier frequency, or sideband selection at the carrier frequency after frequency translation of the baseband signal. For the first approach, sideband selection at baseband followed by frequency translation, the first step is converting the spectrum of the message signal $m(t)$ produced by an audio source from a single-sided (real valued) spectral representation shown in **Figure**

1(a), to a double-sided (complex valued) spectral representation, **Figure 1(b)**. Then, the double-sided representation is filtered by a complex low-pass filter designed to pass the upper sideband, **Figure 2(a)**, or lower sideband, **Figure 2(b)**. The result of passing the double-sided representation, **Figure 1(b)**, through one of the sideband filters, **Figure 2 (a)** or **(b)**, is shown in **Figure**

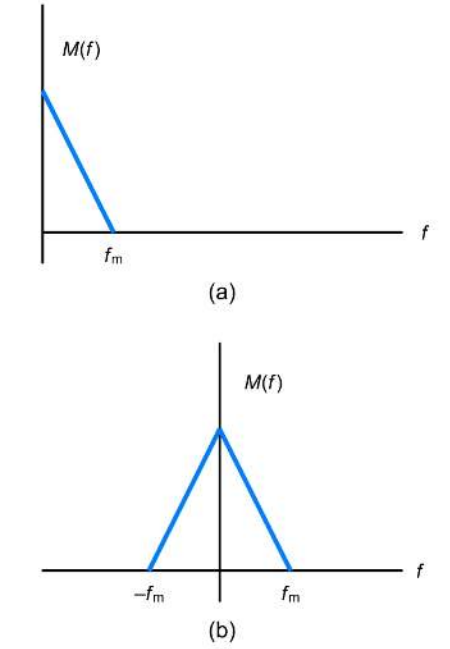

Figure 1 — Notional representations of message spectrum: (a) single-sided (real) representation; (b) double-sided (complex) representation.

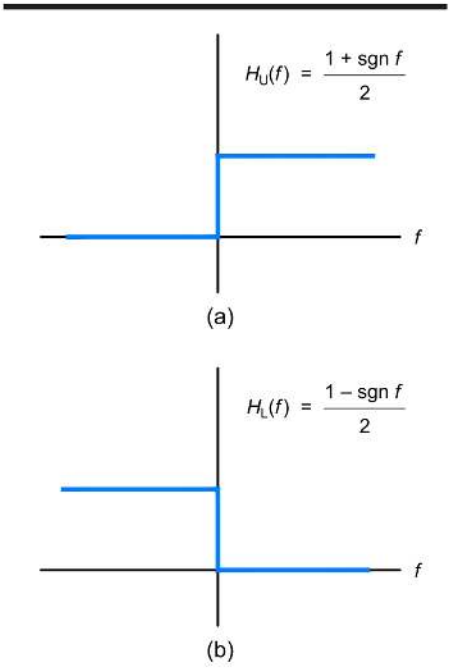

Figure 2 — Transfer function of filter for sideband selection: (a) upper sideband selection; (b) lower sideband selection.

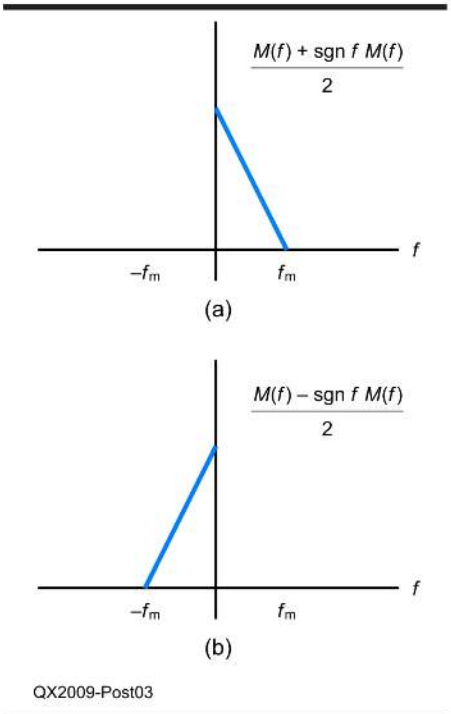

Figure 3 — Message spectrum after sideband filtering: (a) upper sideband spectrum; (b) lower sideband spectrum.

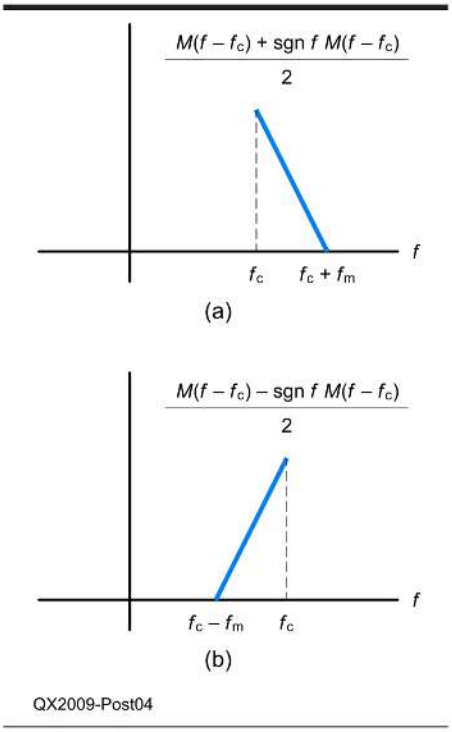

Figure 4 — Message spectrum after filtering and frequency translation: (a) upper sideband translated to carrier frequency; (b) lower sideband translated to carrier frequency.

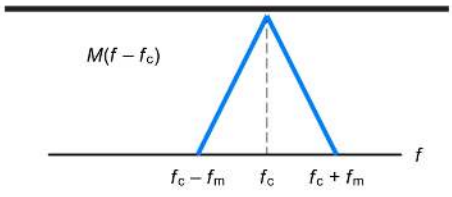

Figure 5 — Double-sided message spectrum representation after frequency translation.

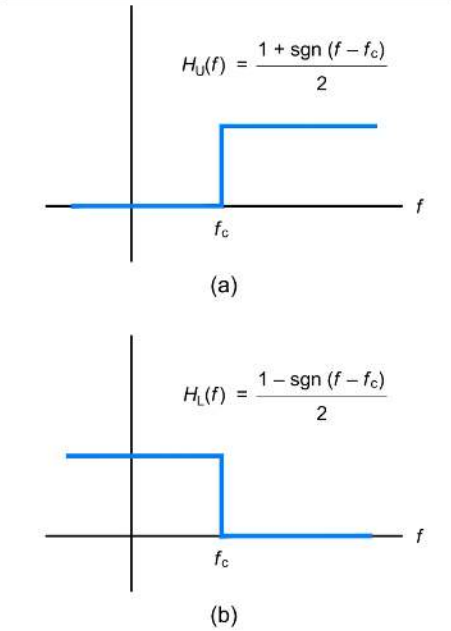

Figure 6 — Filters for sideband selection: (a) upper sideband filter; (b) lower sideband filter.

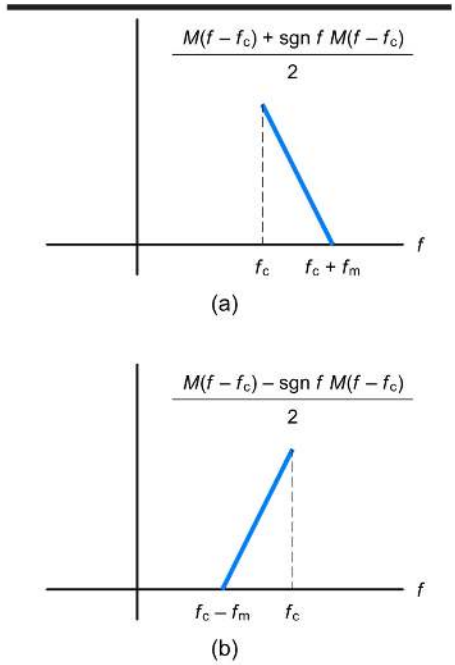

Figure 7 — Spectrum after sideband filtering: (a) upper sideband spectrum; (b) lower sideband spectrum.

3(a) where the upper sideband is selected, and **Figure 3(b)** where the lower sideband is selected. Finally, the desired sideband is translated to the carrier frequency as shown in **Figure 4(a)** or **Figure 4(b)**. **Equation (A7)** in **Appendix 1** demonstrates that the complex representation of the frequency translated SSB signal is

$$x_c(t) = \left(m(t) \pm j\hat{m}(t)\right)e^{j2\pi f_c t}$$

where $\hat{m}(t)$ is the Hilbert transform (a 90° phase shifted version) of $m(t)$ and f_c is the carrier frequency of the translated SSB signal. In **(A7)** the positive sign is taken when representing the upper sideband signal and the minus sign is taken when representing the lower sideband signal. Note that any digital signal processing whose output is equivalent to **(A7)** can generate SSB signals, while any digital signal processing whose output recovers $m(t)$ from **(A7)** can demodulate SSB signals.

Like the first approach, the first step for the second approach is converting the spectrum of the message signal $m(t)$ produced by an audio source from a single-sided (real valued) spectral representation *M(f)* shown in **Figure 1(a)**, to a double-sided (complex valued) spectral representation, **Figure 1(b)**. Then, the double-sideband signal is translated to the carrier frequency as shown in **Figure 5**. Finally, the double-sided representation is filtered by a complex filter designed to pass frequencies below the carrier frequency, **Figure 6(a)**, or frequencies above the carrier frequency, **Figure 6(b)**. The result of passing the double-sided representation, **Figure 1(b)**, through the sideband filters, **Figure 6**, is shown in **Figure 7(a)** where the upper sideband is selected, and **Figure 7(b)** where the lower sideband is selected. **Appendix 1** also demonstrates that the complex representation of the frequency translated SSB signal for the second approach is **(A7)**.

GRC Flowgraph for Audio Recording and Playback

One of the most useful features of *GRC* is the ability to record and play back files containing sampled data using the file source and file sink *GRC* blocks. **Figure 8** depicts a *GRC* flowgraph suitable for recording speech from a microphone to a file. For recording, the upper (record) blocks are enabled, while the lower (playback) blocks are disabled. Then, for playback the upper (record) blocks are disabled while the lower (playback) blocks are enabled. The *GRC* file source block has "repeat" capability, so only a few seconds of recording are necessary to provide audio suitable for SSB transmitter testing. The author's webpage **[8]** provides a sample audio file available to download for demonstration and testing purposes. It is also possible to connect to an external microphone using the audio source block instead of the file source block.

GRC Flowgraphs for Filter Methods

Figure 9 depicts a *GRC* flowgraph that implements the method of SSB generation that performs sideband selection at baseband frequency. The input/output ports for blocks "File Source," "Band Pass Filter", and "Audio Sink" are floating (real valued) representations while the remaining blocks input/output ports are for complex representations. The file source block provides recorded audio for testing and the audio sink makes it audible from the PC speaker. A GUI chooser block designates the variable **Sideband_select** for sideband selection with default value of 0 for upper sideband selection, or 1 for lower sideband selection.

Figure 10 displays the band-pass filter properties required to perform sideband selection at baseband frequencies. The "FIR Type" selection is set to convert floating (real valued) representations to complex representations with complex taps selected to permit asymmetric filtering of positive and negative frequencies. Only one sideband filter is necessary because of the use of mathematical expressions for the low and high cutoff frequencies for the filter. Selection of the upper sideband choice results in **Sideband_select = 0** and the low and high frequency cutoff expressions evaluate to 300 Hz and 3000 Hz, respectively. Selection of the lower sideband choice results in **Sideband_select = 1** and the low and high cutoff frequency expressions evaluate to –3000 Hz and –300 Hz, respectively.

The rational resampler block in **Figure 9** converts the 36 KSPS (kilosamples per second) audio rate to a 360 KSPS rate before further processing. The signal source block produces a complex exponential that multiplies the chosen sideband in order to translate it anywhere from 0 Hz to 350 kHz higher in frequency as established by the user selectable variable **Frequency**. The resulting complex samples are written to a file by the file source block. Two FFT

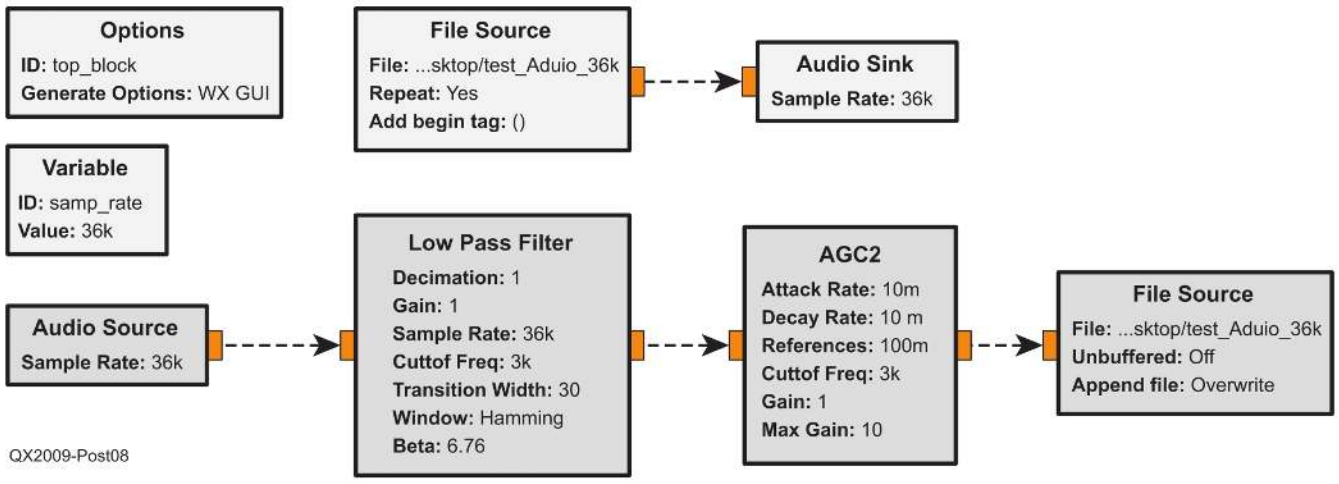

Figure 8 — *GRC* flowgraph for recording and playback of audio files at 36 KSPS. "File Source" and "Audio Sink" blocks are disabled in this flowgraph, remaining blocks are enabled.

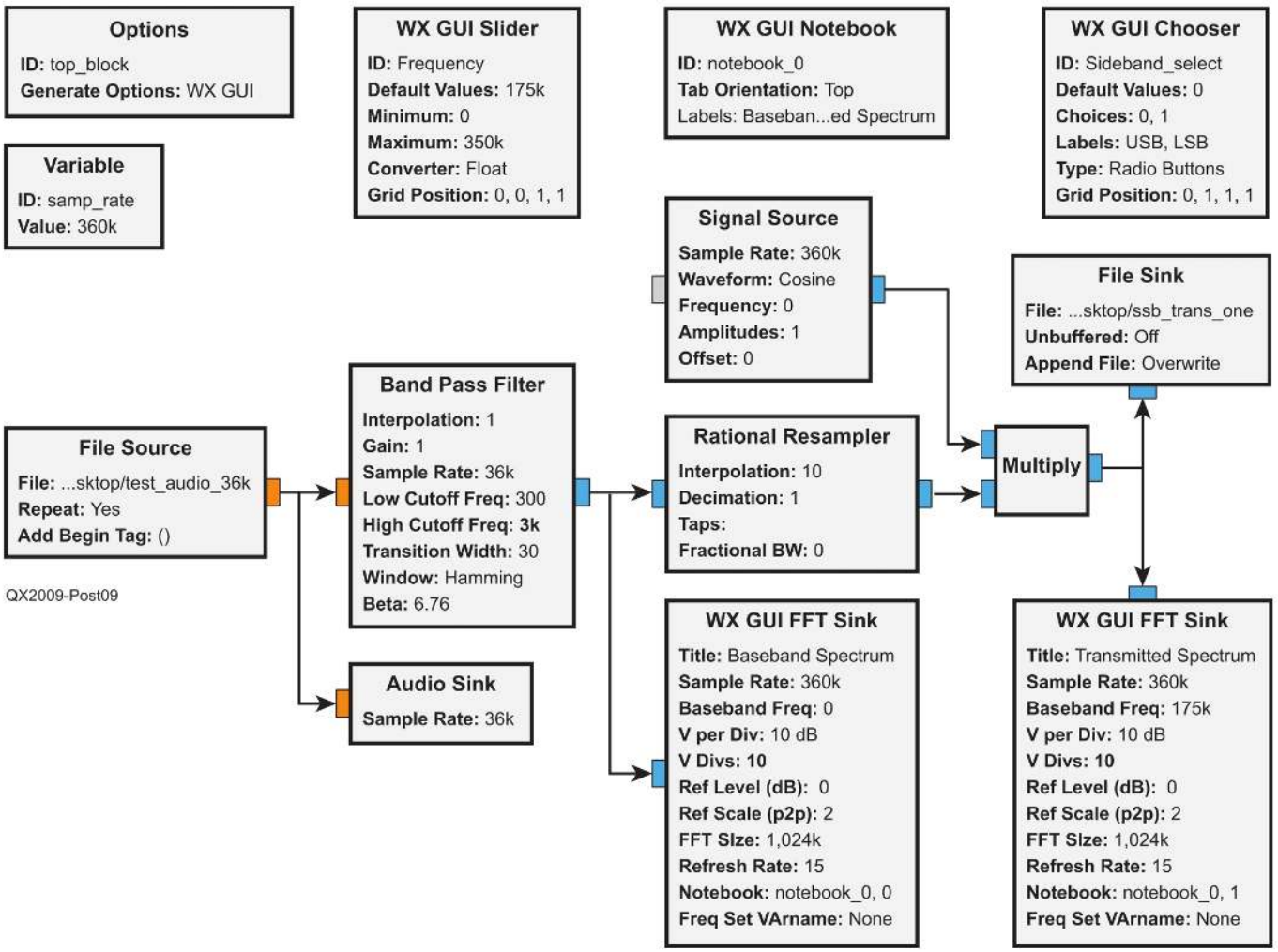

Figure 9 — *GRC* flowgraph for sideband generation with baseband frequency filtering.

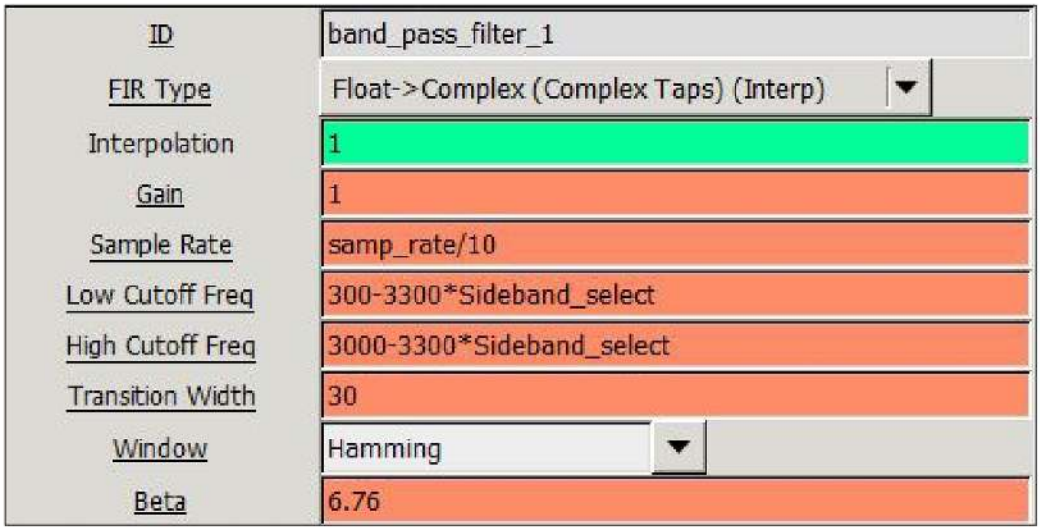

Figure 10 — Band-pass filter properties that show conversion from real (float) to complex filtering. Complex taps selection permits asymmetric filtering of positive or negative frequencies.

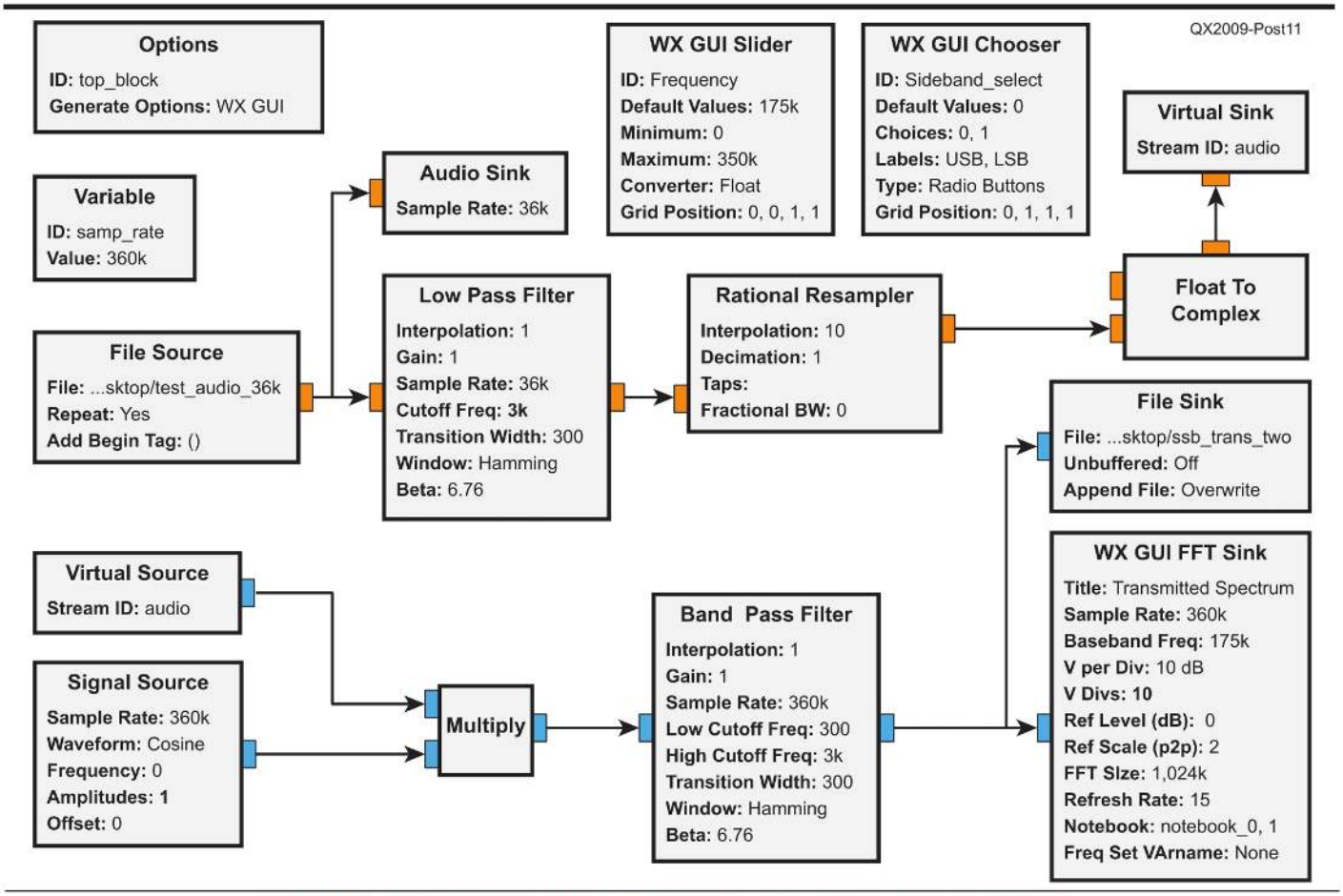

Figure 11 — *GRC* flowgraph for sideband generation with carrier frequency filtering.

sink blocks graphically display the selected sideband at baseband, as well as the selected sideband at the up-converted frequency. As stated previously, the *GRC* file source block has "repeat" capability, so only a few seconds of generated SSB signals are necessary to provide signals for testing the SSB receivers described in upcoming sections.

Figure 11 depicts a *GRC* flowgraph that implements the method of SSB generation that performs sideband selection at carrier frequency. The input/output ports for the blocks "File Source," "Low Pass Filter," "Audio Sink," "Rational Resampler," and input to "Float To Complex" are floating (real valued) representations, while the remaining blocks input/output ports are complex representations.

As in the previous flowgraph, the file source block provides recorded audio for testing and the audio sink makes it audible from the PC speaker. The rational resampler block converts the 36 KSPS audio rate to a 360 KSPS rate before conversion from float (real valued) to complex valued by the float to complex block. A GUI chooser block designates the variable **Sideband_select** for sideband selection with default value

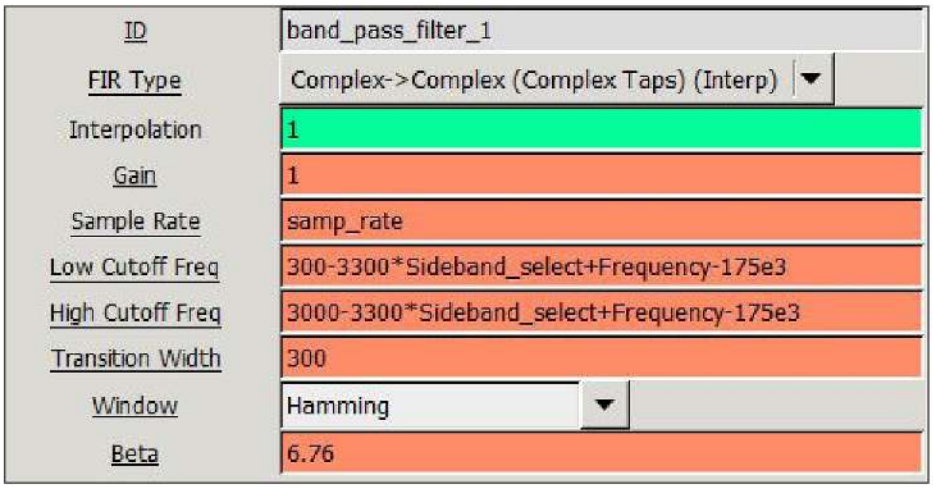

Figure 12 — Band-pass filter properties for carrier frequency filtering. Complex taps selection permits asymmetric filtering of positive or negative frequencies. Low and high cutoff frequencies are selected to filter at carrier frequency rather than at baseband frequency.

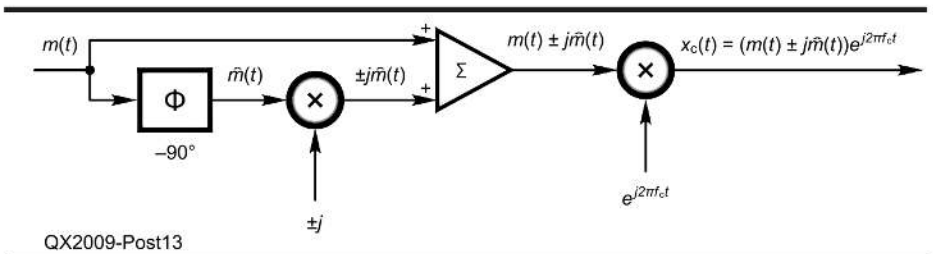

Figure 13 — Phase-shift SSB modulator.

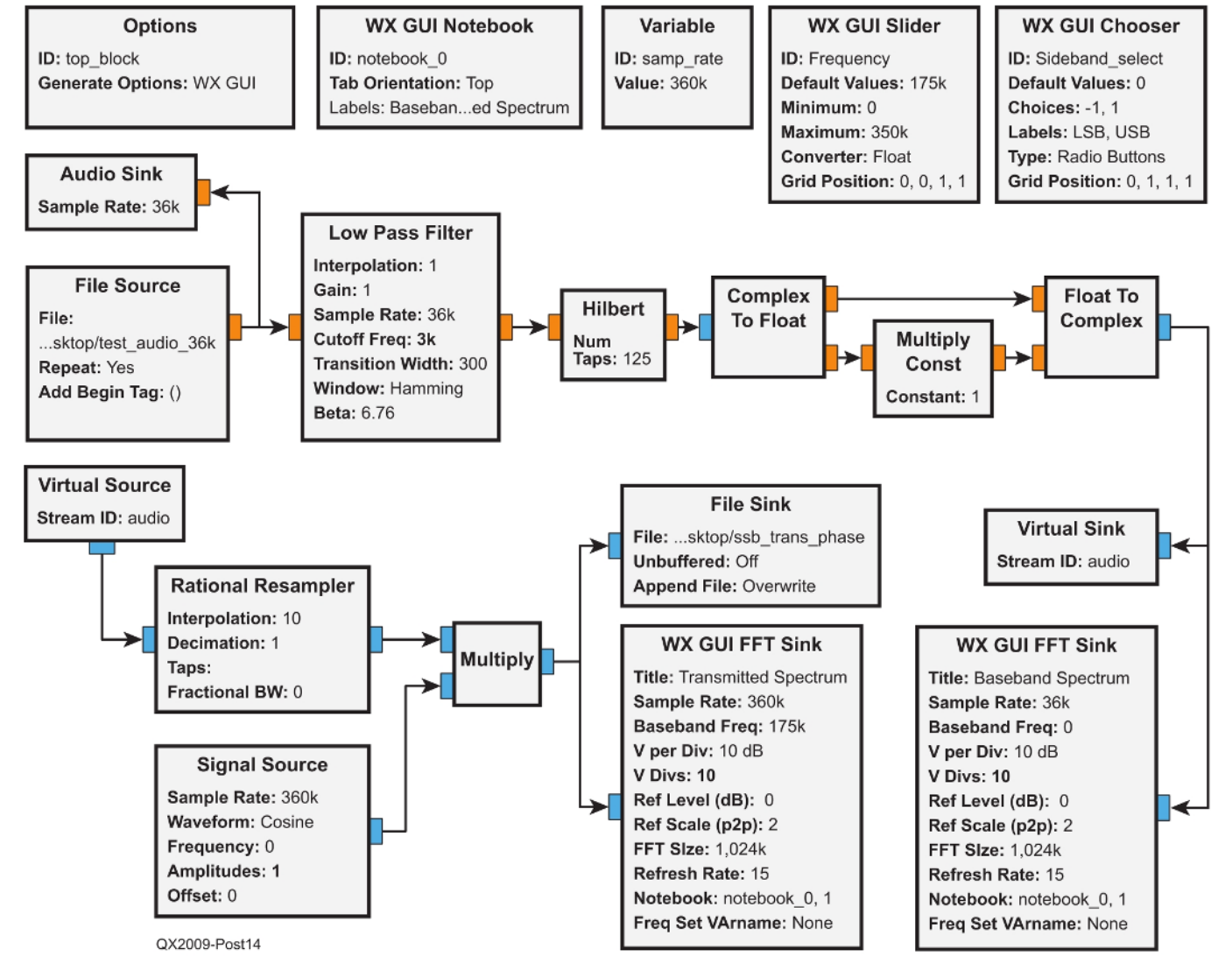

Figure 14 — *GRC* flowgraph for sideband generation using the phasing method.

of 0 for upper sideband selection, or 1 for lower sideband selection. The signal source block produces a complex exponential that multiplies the sidebands in order to translate them anywhere from 0 Hz to 350 kHz higher in frequency as established by the user selectable variable **Frequency**.

Figure 12 displays the band-pass filter properties required to perform sideband selection at the carrier frequency. The "FIR Type" selection is set for complex filtering with complex taps selected to permit asymmetric filtering of positive and negative frequencies. Once again, only one sideband filter is necessary because of the use of mathematical expressions for the low and high cutoff frequencies for the filter. Selection of the upper sideband choice results in **Sideband_select = 0** and the low and high frequency cutoff expressions evaluate to the carrier frequency +300 Hz and the carrier frequency +3,000 Hz, respectively. Selection of the lower sideband choice results in **Sideband_select = 1** and the low and high cutoff frequency expressions evaluate to the carrier frequency –3,000 Hz and the carrier frequency –300 Hz, respectively. The 175 kHz offset is necessary to account for the fact that while frequencies computed by the FFT range from –175 kHz to 175 kHz, displayed frequencies should range from 0 to 350 kHz.

Phase-shift Method of SSB Generation

Figure 13 displays a phase shift modulator for generating SSB. The message signal $m(t)$ is summed with a 90° degree phase shifted version (or Hilbert transformed version) of $m(t)$ that has been multiplied by $\pm j$ to form $\left(m(t) \pm j\hat{m}(t)\right)$. In this complex expression the plus sign is taken when selecting the upper sideband, while the minus sign is taken when selecting the lower sideband. The complex version of the modulating waveform is multiplied by a complex exponential with frequency f_c in order to translate the sideband to the carrier frequency. As stated previously, because the signal produced by this process shown in **Figure 13** is identical to **Equation (A7)**, the phase shift modulator produces SSB signals.

GRC Flowgraph for Phase-shift Method

Figure 14 depicts a *GRC* flowgraph that applies the phase-shift method to generate SSB modulation. A Hilbert transform block creates a complex expression with real part $m(t)$ and imaginary part $\hat{m}(t)$. This is

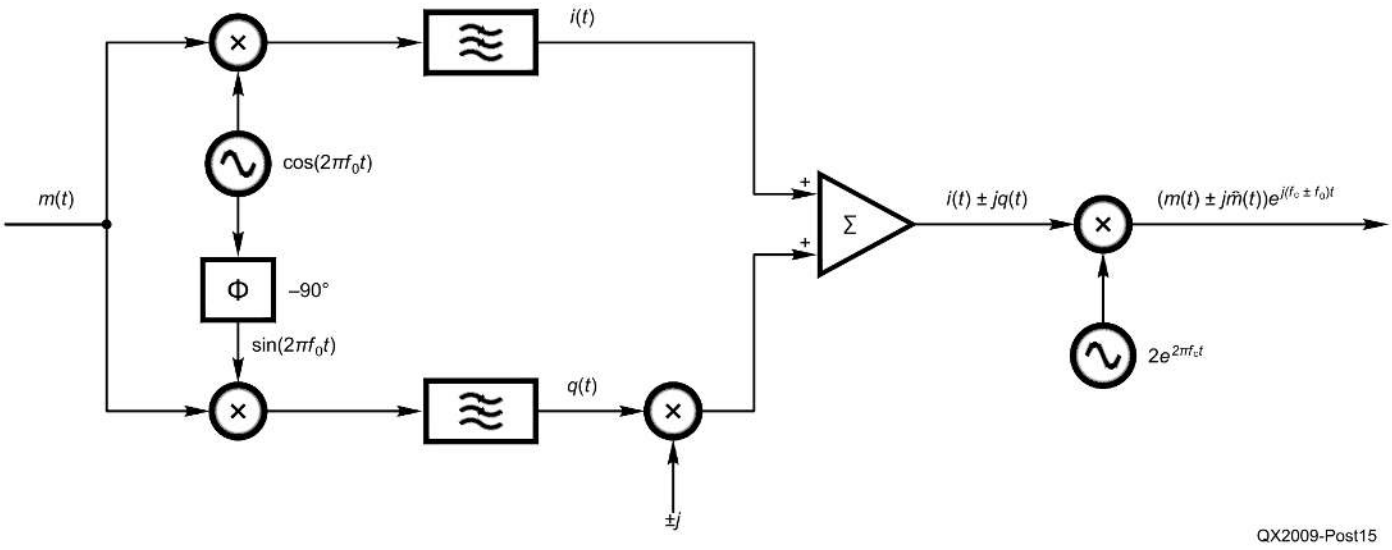

Figure 15 — Weaver SSB modulator.

followed by complex to float and float to complex blocks that break out the imaginary component to permit multiplication by the variable **Sideband_select** for sideband selection with default value of +1 for upper sideband selection, or –1 for lower sideband selection. The rational resampler block converts the 36 KSPS audio rate to a 360 KSPS rate before multiplication by a complex exponential with frequency f_c produced by the signal source block. Multiplication translates the chosen sideband anywhere from 0 Hz to 350 kHz higher in frequency as established by the user selectable variable **Frequency**. The resulting complex samples are written to a file by the file source block. Two FFT sink blocks graphically display the selected sideband at baseband, as well as the selected sideband at the carrier frequency.

Weaver's Method of SSB Generation

Figure 15 depicts Weaver's method of SSB generation. This method applies the message signal $m(t)$ to a pair of multipliers with the top multiplier being driven directly by an oscillator with audio frequency f_0, while the bottom multiplier is driven by the oscillator signal phase shifted by –90°. After low pass filtering the outputs are added to produce the lower sideband, or subtracted to produce the upper sideband. **Appendix 2** demonstrates that the complex representation of the frequency translated SSB signal for Weaver's method is **Equation (A23)**

$$x_c(t) = \left(m(t) \pm j\hat{m}(t)\right)e^{j2\pi\left(f_c \mp \frac{f_m}{2}\right)t}$$

Comparing **(A23)** with **(A7)** demonstrates that the transmitted frequency for Weaver's method is offset $f_m/2$ below the carrier frequency f_c when transmitting the upper sideband, and offset $f_m/2$ above the carrier frequency f_c when transmitting the lower sideband. These frequency offsets may be corrected by adding $f_m/2$ to the transmit frequency when transmitting the upper sideband, and subtracting $f_m/2$ from the transmit frequency when transmitting the lower sideband.

GRC Flowgraph for Weaver's Method

Figure 16 depicts a *GRC* flowgraph that applies Weaver's method to generate SSB modulation. The message signal $m(t)$ is fed to a pair of multipliers that are also fed a complex 1.5 kHz audio signal split into quadrature signals by a complex to float block. The outputs of the multipliers are low-pass filtered and converted from float (real valued) to complex valued prior to the rational resampler block converting the 36 KSPS audio rate to a 360 KSPS rate. The gain term of the lower filter is set by the variable **Sideband_select** for sideband selection with default value of –1 for upper sideband selection, or +1 for lower sideband selection. Multiplication of the complex signal by a complex exponential produced by the signal source block translates the chosen sideband anywhere from 0 Hz to 350 kHz higher in frequency as established by the user selectable variable **Frequency**. Finally, the complex samples are written to a file by the file source block. Two FFT sink blocks graphically display the selected sideband at baseband, as well as the selected sideband at the carrier frequency. **Figure 17** shows the method for correcting the frequency offset produced by Weaver's method.

Figure 18 compares the baseband frequency spectrum of the SSB modulation produced by the filter and phasing methods with the baseband frequency spectrum produced by Weaver's method. Understanding the difference between these two spectra will prove helpful in the next section, which discusses reception of SSB signals generated by the methods discussed above.

Filter Method of SSB Reception

Conceptually, SSB reception occurs by translating the upper sideband, **Figure 4(a)**, or the lower sideband, **Figure 4(b)**, down to baseband, **Figures 3(a)** and **3(b)**, respectively. This can occur either through multiplication by a complex exponential signal source when the frequency is set to the negative of the carrier frequency, $-f_c$, or using the frequency xlating FIR filter block. The frequency xlating FIR block translates complex samples at the carrier frequency produced either by a hardware source or a file source down to baseband for further processing. The frequency xlating FIR block also includes a low pass filter whose width must be set to $2f_m$ to pass both sidebands shown in **Figure 18(a)**, or whose

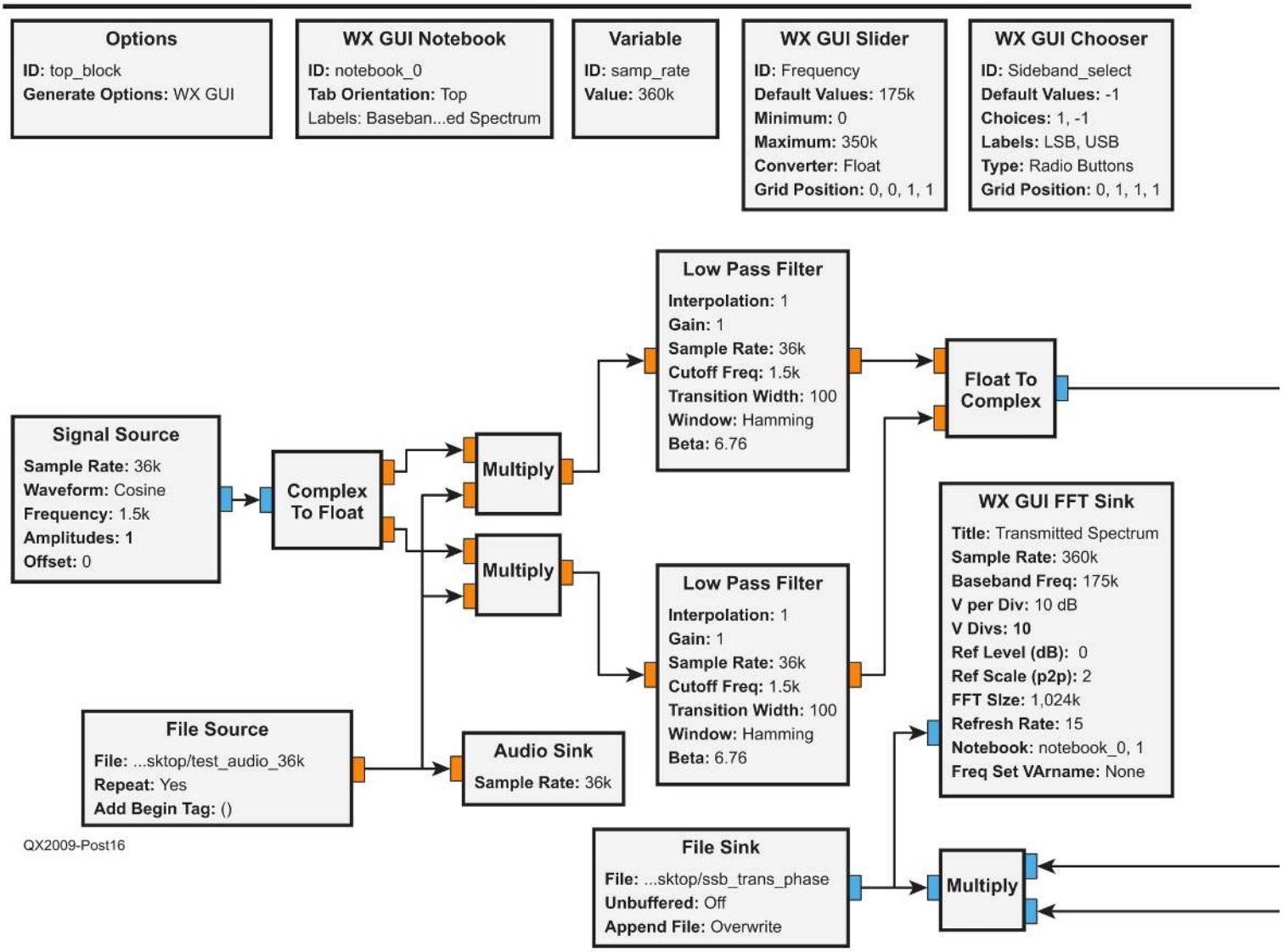

Figure 16 — *GRC* flowgraph for sideband generation using Weaver's method.

Figure 17 — Complex exponential source properties depicting method of offset frequency selection.

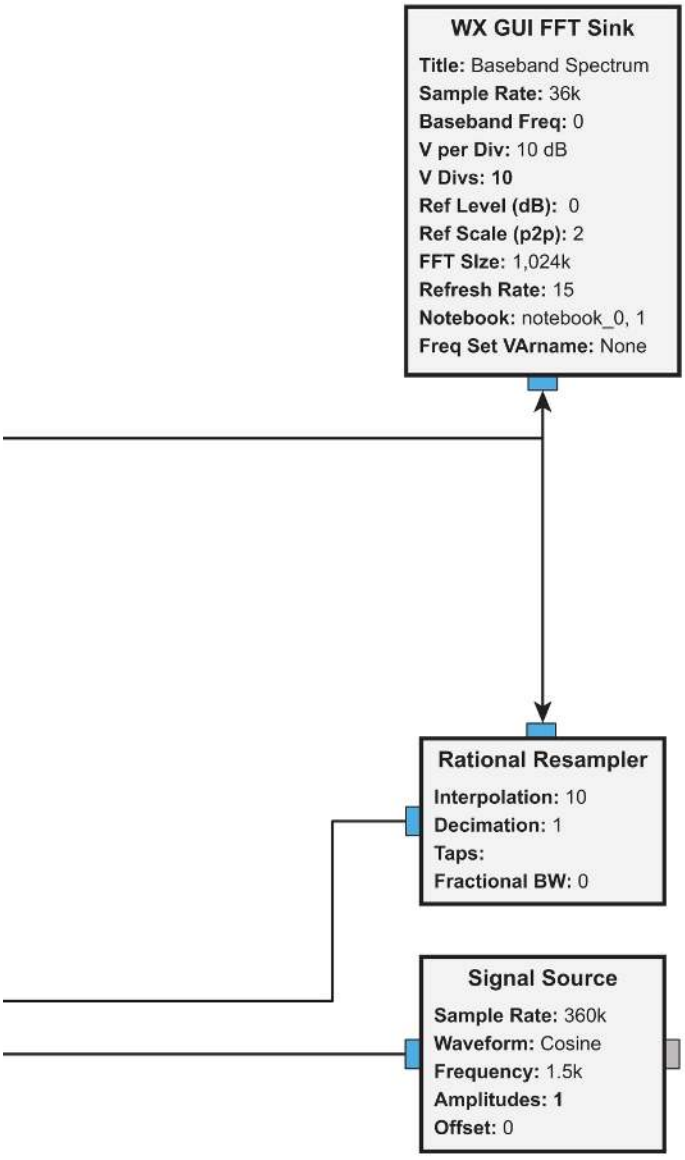

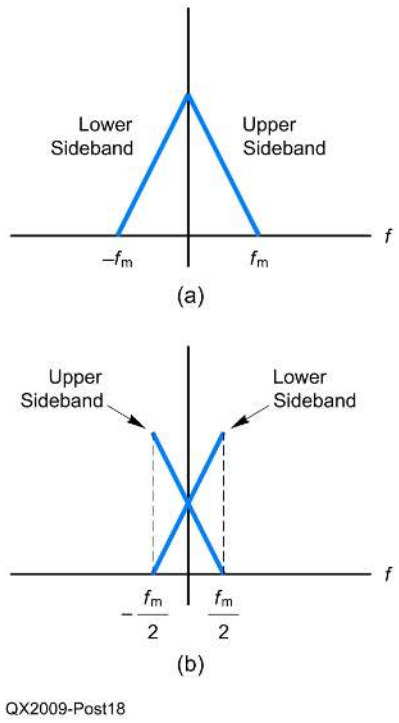

Figure 18 — Message spectrum representations: (a) sideband spacing at baseband produced by filter and phasing methods; (b) sideband spacing at baseband produced by Weaver's method.

width must be set to f_m to pass the sideband configuration shown in **Figure 18(b)**.

Mathematically speaking, either method of frequency translation is equivalent to multiplying both sides of **Equation (A7)** by a complex exponential with frequency $-f_c$ to give

$$x_c(t)e^{-j2\pi f_c t} = \left(m(t) \pm j\hat{m}(t)\right)e^{j2\pi f_c t}e^{-j2\pi f_c t} = m(t) \pm j\hat{m}(t) \quad (1)$$

The final step is to employ the complex-to-float block to separate out either the real part of **(1)** — the message signal, $m(t)$ — or the imaginary part of **(1)** — the Hilbert transformed message signal, $\hat{m}(t)$ for reproduction as an audio waveform.

Figure 19 depicts a *GRC* flowgraph that implements the minimum SSB receiver that applies these concepts. The SDRplay RSP1 block (shown as disabled on the flowgraph) provides complex signal samples from 10 kHz to 2 GHz at bandwidths up to 10 MHz through a cable connected to the PC USB port, but other hardware choices are possible **[9]**. In this case, the "File Source" block is enabled to play a recorded data file containing complex samples produced by one of the SSB generation methods discussed above, or other recorded files as discussed below. The "AGC2" (automatic gain control block) provides up to 65536 times gain (about 96 dB) to attempt to keep the signal near the reference level, 0.2 in this application. The "Multiply Const" block implements manual gain controlled by a GUI slider. The "Audio Sink" block directs sound samples to the sound card in the PC and then on to the speaker.

A shortcoming of the SSB receiver shown in **Figure 19** is the inability to select a desired sideband and reject the noise and interference in the undesired sideband. **Figure 20** depicts a modified *GRC* flowgraph of a SSB receiver that employs a complex band-pass filter that permits sideband selection. A "WX GUI Chooser" block designates the variable **Sideband_select** for sideband selection with default value of 0 for upper sideband selection, or 1 for lower sideband selection. Once again, only one sideband filter is necessary because of the use of mathematical expressions for the low and high cutoff frequencies for the filter, **Figure 21**. Selection of the upper sideband choice results in **Sideband_select =** 0 and the low and high frequency cutoff expressions evaluate to 300 Hz and 3,000 Hz, respectively. Selection of the lower sideband choice results in **Sideband_select = 1** and the low and high cutoff frequency expressions evaluate to –3,000 Hz and –300 Hz, respectively.

Figure 22 depicts the *GRC* SSB receiver in action with a sample file recorded by the SDR Play RSP1 during the WPX contest held in March, 2020. Data files recorded during the contest for both lower sideband, recorded on 40 meters, and upper sideband, recorded on 20 meters, are available on the author's webpage **[8]**.

Note that because $\hat{m}(t)$ is a 90° phase shifted version of *m (t)*, no audible difference between the two signals is discernible. To demonstrate, this set **num inputs = 2** in the property box of

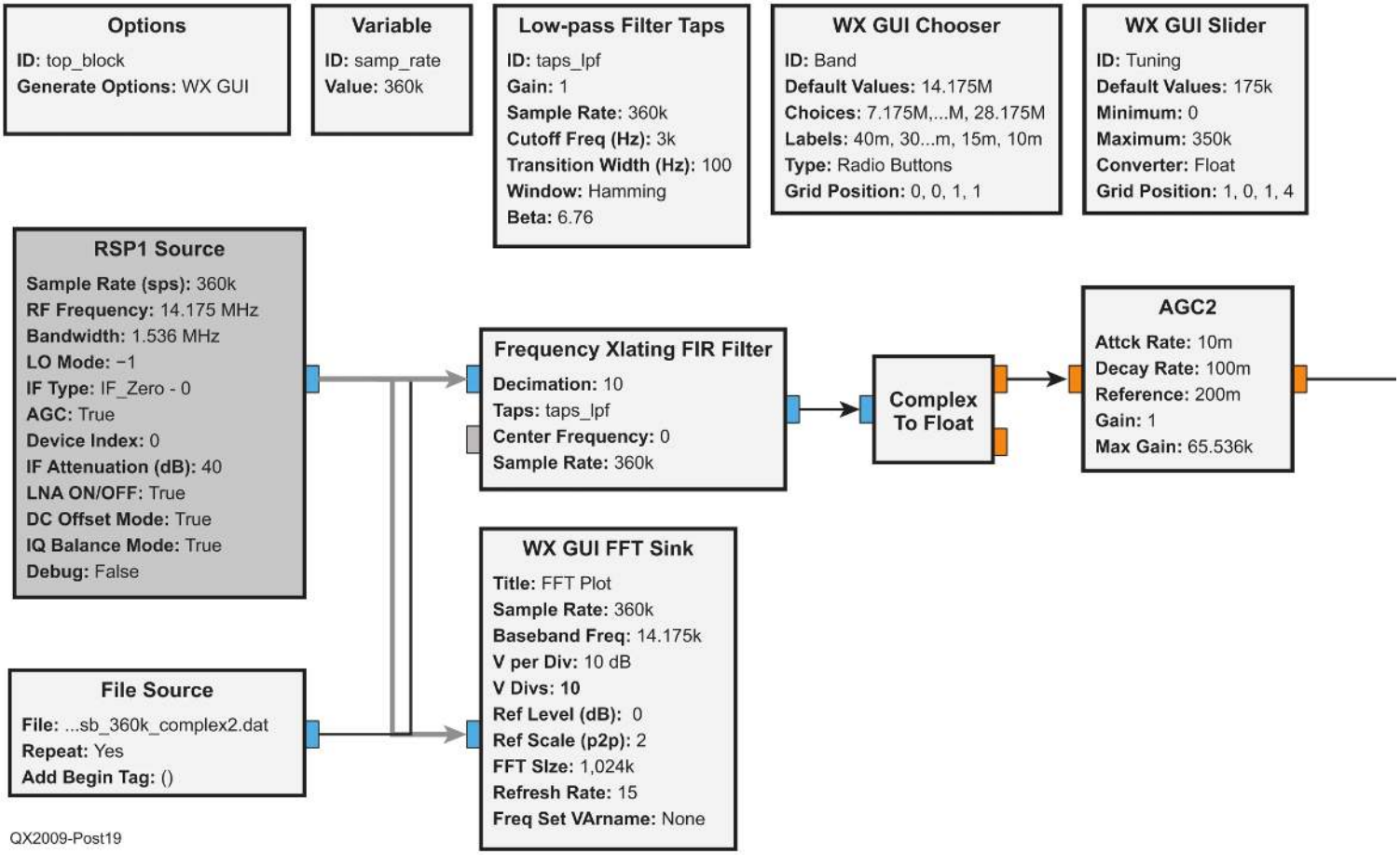

Figure 19 — *GRC* flowgraph for a minimum SSB receiver without sideband selection capability.

the audio sink to accommodate stereo signals. Then, construct a duplicate path from the imaginary output of the complex-to-float block to the 2nd audio input that mirrors the path from the real output of the complex-to-float block to the 1st audio input. This produces a stereo audio signal with $m(t)$ on one channel, and $\hat{m}(t)$ on the other channel. No difference is noticeable between them when listening to the stereo audio, even with headphones.

The AGC blocks in the SSB receivers are so effective that the non-selected sideband will become audible when testing SSB generation methods. The ~96 dB gain of the AGC easily overcomes the 50 to 60 dB attenuation provided by the sideband filter.

Weaver's Method for SSB Reception

A method that appears analogous to Weaver's method of SSB generation can be applied to the task of SSB reception. This method begins by using the frequency xlating FIR filter block to translate the upper sideband, **Figure 4(a)**, or the lower sideband, **Figure 4(b)**, down to baseband with a frequency offset, **Figure 18(b)**. Mathematically speaking, this frequency translation is equivalent to multiplying both sides of **Equation (A23)** by a complex exponential with frequency $-f_c$ to give

$$x_c(t)e^{-j2\pi f_c t} = \left(m(t) \pm j\hat{m}(t)\right)e^{j2\pi\left(f_c \mp \frac{f_m}{2}\right)t}e^{-j2\pi f_c t} = \left(m(t) \pm j\hat{m}(t)\right)e^{\mp j2\pi\left(\frac{f_m}{2}\right)t} \quad (2)$$

Next, the right-hand side of **(2)** is multiplied by a complex exponential with frequency $+f_m/2$ for upper sideband selection, or $-f_m/2$ for lower sideband selection

$$\left(m(t) \pm j\hat{m}(t)\right)e^{\mp j2\pi\frac{f_m}{2}t}e^{\pm j2\pi\frac{f_m}{2}t} = m(t) \pm j\hat{m}(t) \quad (3)$$

As before, the "Complex To Float" block is employed to separate out the real part of **(3)** containing the message waveform $m(t)$; then applying automatic and manual gain blocks followed by the audio sink block to make the sound audible.

Figure 23 depicts a *GRC* flowgraph of a SSB receiver inspired by Weaver's method. The frequency xlating FIR filter block translates the carrier frequency to baseband to produce the spectrum shown in **Figure 18(b)**. Sideband selection is achieved by shifting this spectrum up or down in frequency by multiplying by a ±1.5 kHz complex exponential signal produced by the signal source block. A GUI chooser block designates the variable **Sideband_select** for sideband selection with default value of +1 for upper sideband

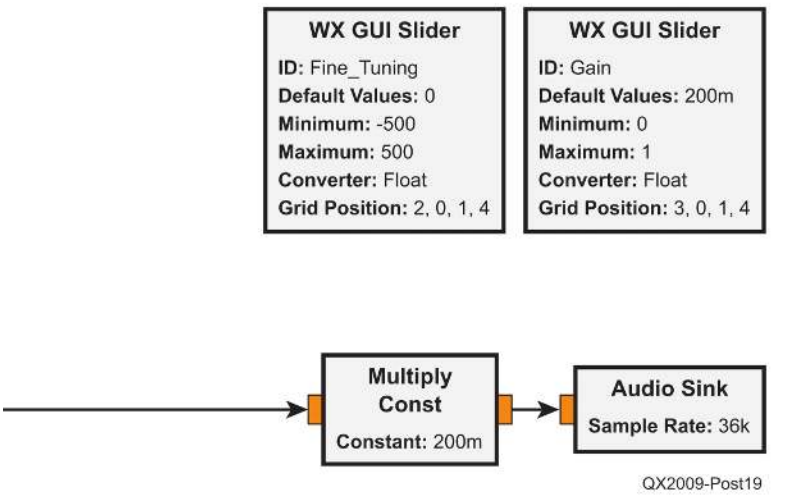

selection, or −1 for lower sideband selection. **Figure 24** shows the mathematical expression in the signal source properties window using the variable **Sideband_select** to offset the frequency by ±1.5 kHz for sideband selection.

Hardware Demonstration of SSB Signal Generation and Reception Using ADALM-PlutoSDR

The Analog Devices Active Learning Module-Pluto Software Defined Radio or ADALM PlutoSDR is based on the Analog Devices AD9363 RF agile transceiver device, **Figure 25**, see **[10, 11]**. PlutoSDR has a compact form-factor, is USB powered, and can be controlled by a variety of software packages through USB including *GNU Radio Companion*. It is possible to open a serial connection to PlutoSDR and issue commands that extends the tuning range from 70 MHz to 6 GHz and the bandwidth to 56 MHz using the AD9364 configuration, rather than the default AD 9363 configuration that provides a tuning range from 325 MHz to 3.8 GHz and a bandwidth of 20 MHz **[12]**.

Unfortunately, PlutoSDR source and sink blocks are only available in the Linux-based version of *GRC*. Fortunately, a convenient way of using this version of *GRC* on any PC is to use a bootable USB flash drive imaged with the *GNU Radio Live SDR Environment*, see **[13]**. After restarting the PC and booting from the USB drive it is possible to download and install the "gr-iio" blocks that contain the source and sink *GRC* radio modules that interface with PlutoSDR **[14]**. Once this is done, layout of *GRC* flowgraphs is identical to the process used with the PC version of *GRC*.

Figure 26 depicts a *GRC* flowgraph that implements a 70 cm SSB transceiver using an ADALM-PlutoSDR. The upper portion of the flowgraph implements the sideband selection using the baseband filtering method of SSB generation. The desired sideband is multiplied by a complex exponential tunable from 0 – 100 kHz in order to vary the PlutoSDR carrier frequency from 430 MHz to 430.1 MHz — of course, other choices are possible. The lower portion of the flowgraph implements the filter method of SSB reception as previously described in the section on SSB receivers. Two FFT blocks allow visual comparison of the transmitted and received baseband waveforms.

One other note concerning PlutoSDR is relevant — the PlutoSDR sink block does not permit disabling the transmitter, but it is possible to attenuate the transmitted signal in 0.25 dB steps by up to 89.75 dB. This reduces the power of the transmitted signal below the threshold of audibility at the receiver. In this application, during normal operation the transmit power is attenuated by 50 dB to avoid overload at the receiver. It is possible to replace the file source block with an audio sink block in order to use a microphone to transmit voice instead of a recorded audio file. The audio source block is shown in dark gray in **Figure 26**, indicating that it has been disabled in favor of the file source block.

Conclusion

This article shows that it is possible to implement legacy SSB generation and reception methods using *GRC* software. A 70-cm PlutoSDR transceiver was presented to demonstrate that it is possible to communicate with inexpensive SDR platforms controlled by *GRC*. I hope what I have presented here motivates you to investigate further how to apply *GNU Radio Companion* to the task of generating and receiving SSB signals.

Appendix 1

The complex representation of the SSB signal is developed by applying principles from signals and systems theory. For the derivations presented here, sideband filtering is accomplished using multiplication in the frequency (Fourier) domain, while frequency translation is accomplished using multiplication in the time domain. The transfer function for the upper sideband filter, **Figure 2(a)** is expressed as

$$H_U(f) = \frac{1+\text{sgn}f}{2} \tag{A1}$$

while the transfer function for the lower sideband filter, **Figure 2(b)** is expressed as

$$H_L(f) = \frac{1-\text{sgn}f}{2} \tag{A2}$$

where the sgn function ("read signum f") is defined as

$$\text{sgn}\, f = \begin{cases} 1, f > 0 \\ 0, f = 0 \\ -1, f < 0 \end{cases} \tag{A3}$$

Expressed in a compact way, the sideband filter transfer functions are

$$H(f) = \frac{1 \pm \text{sgn}f}{2} \tag{A4}$$

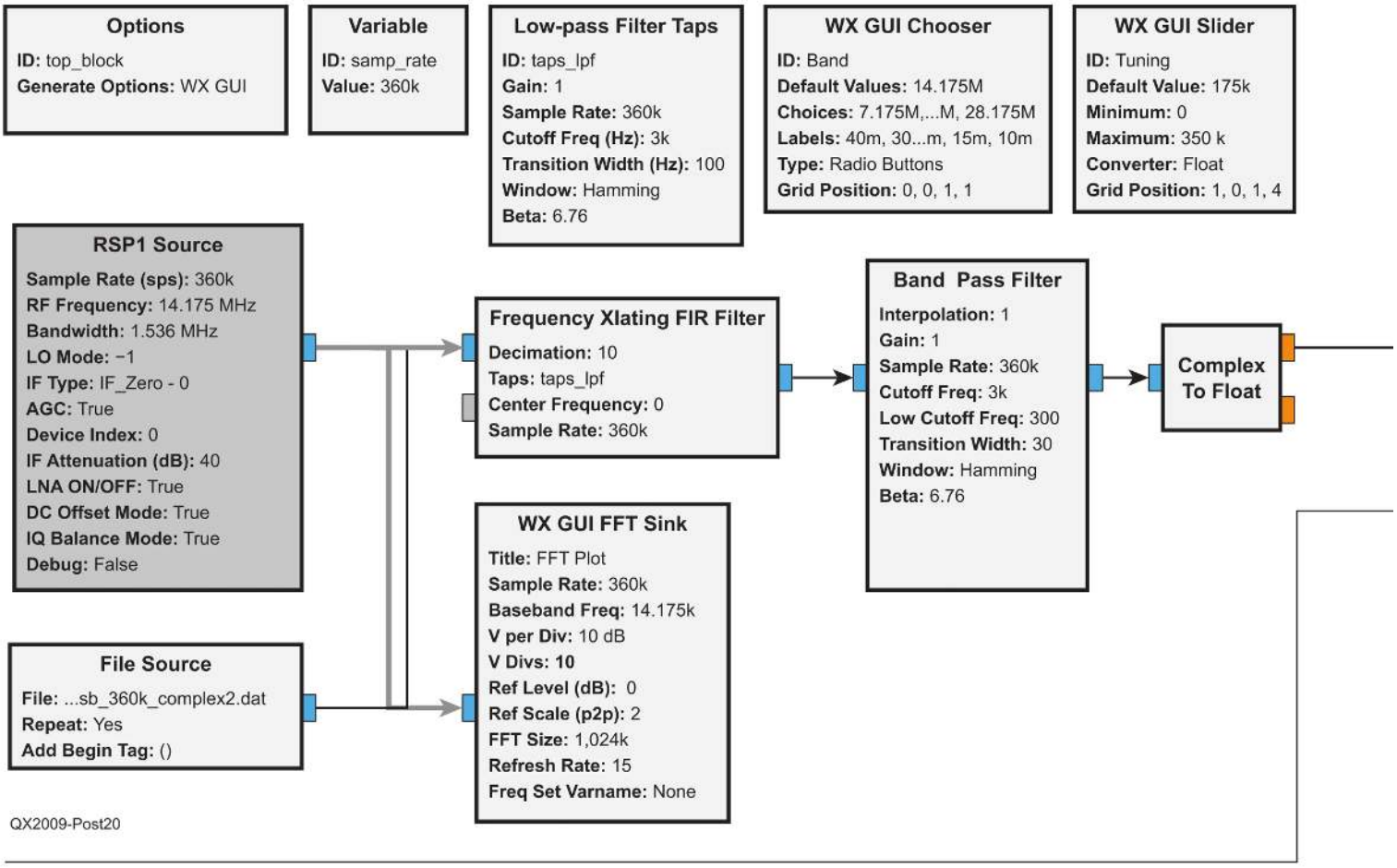

Figure 20 — *GRC* flowgraph of SSB receiver that includes sideband selection capability.

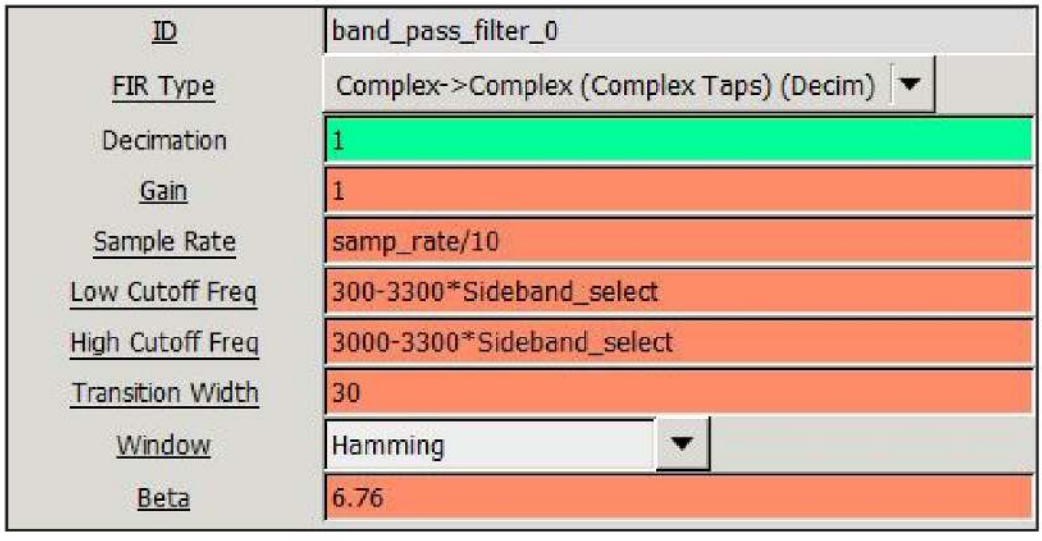

Figure 21 — Band-pass filter properties for sideband selection. Complex taps selection permits asymmetric filtering of positive or negative frequencies.

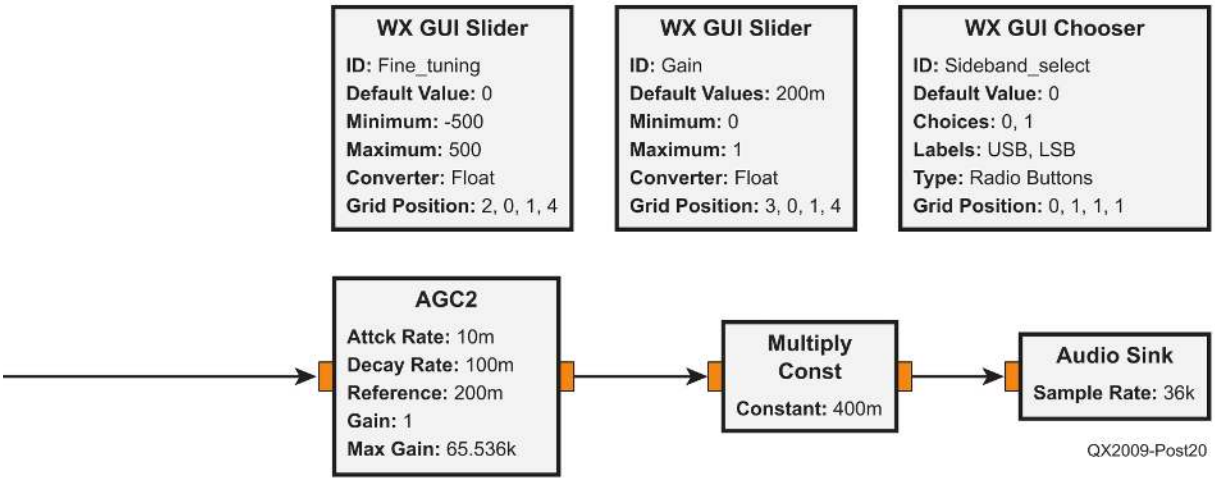

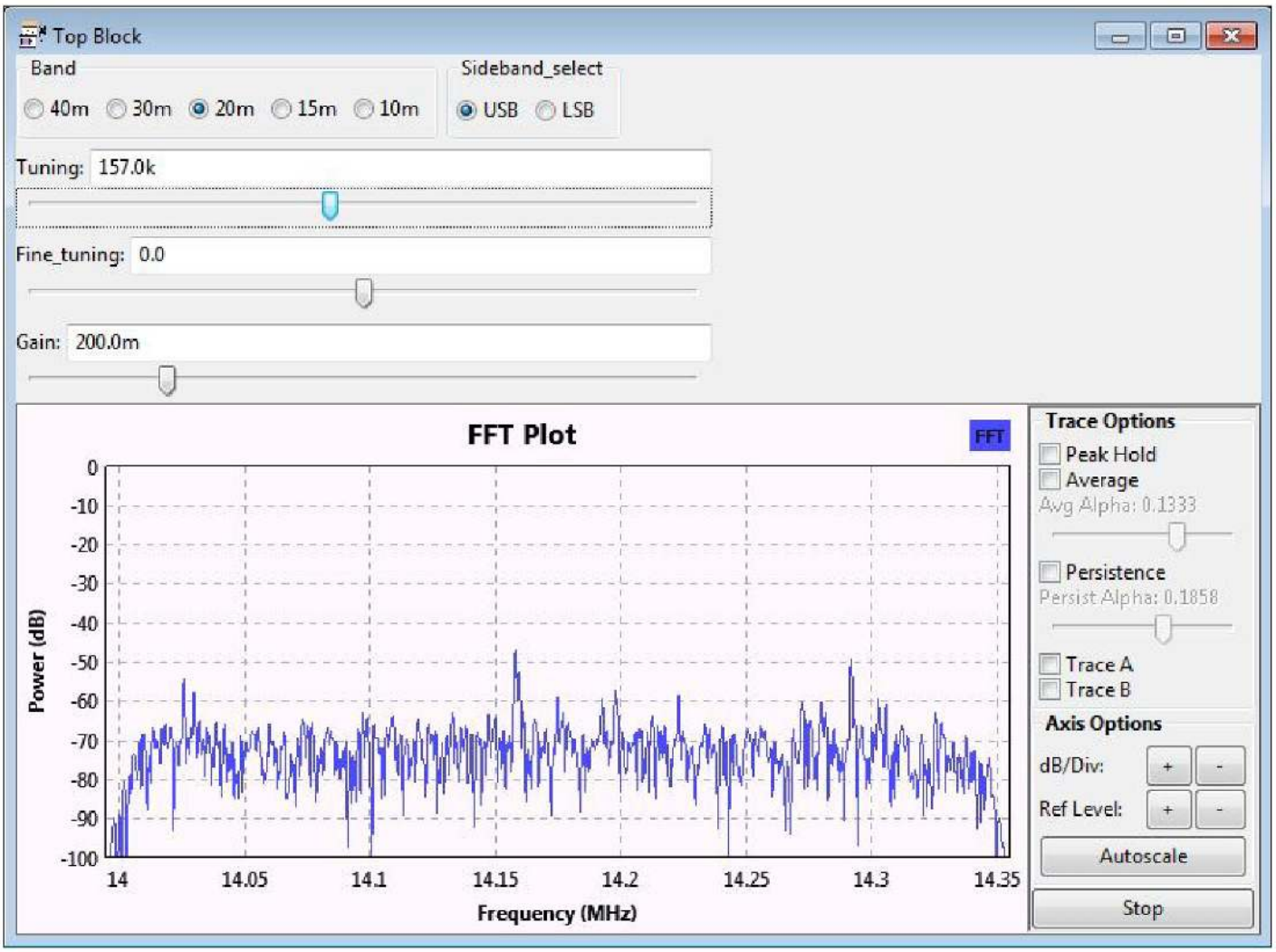

Figure 22 — Screen capture of *GRC* SSB receiver demodulating a recorded data file.

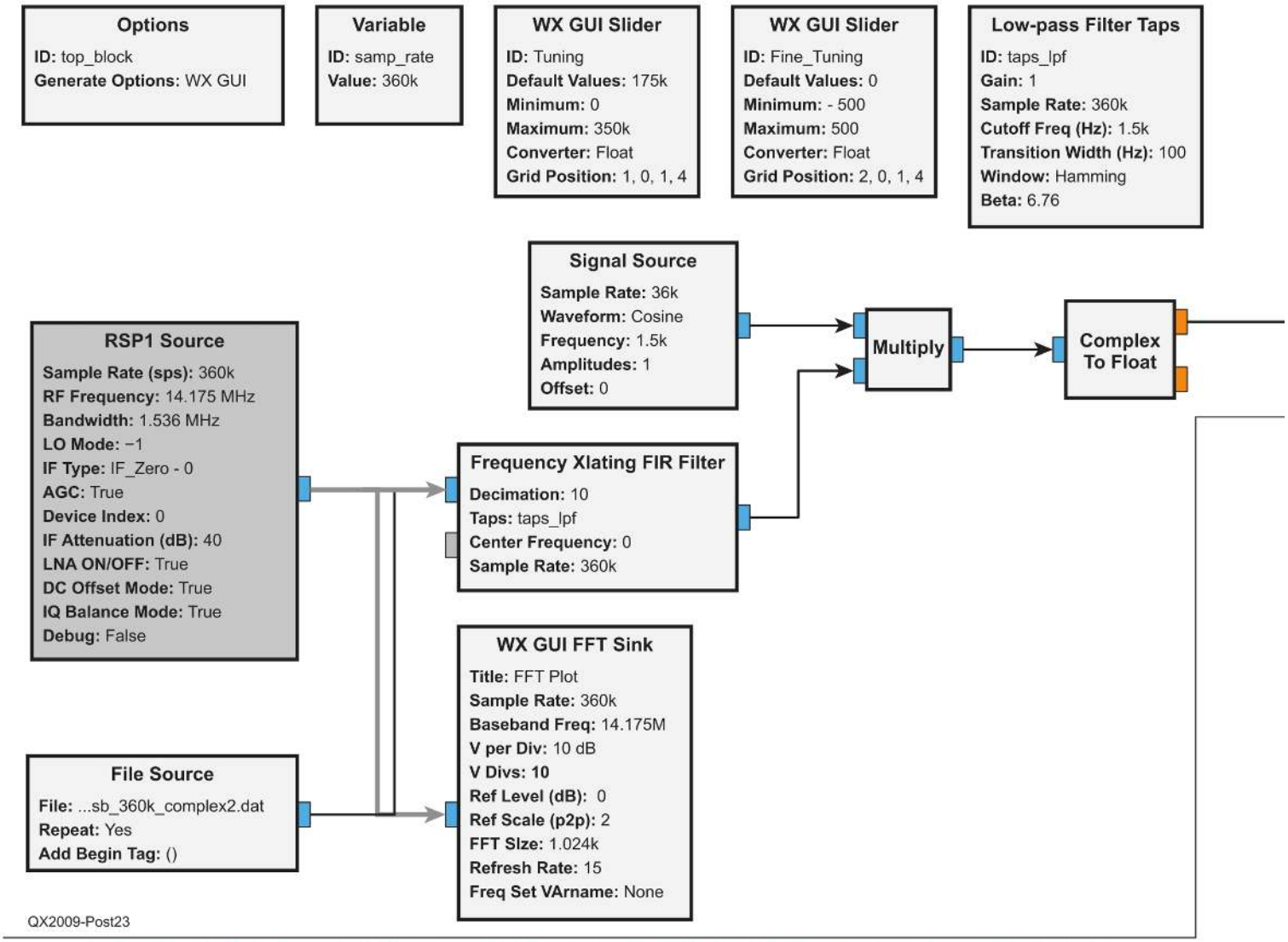

Figure 23 — *GRC* flowgraph of SSB receiver inspired by Weaver's method that includes sideband selection capability.

where the upper sign is taken when selecting the upper sideband, while the lower sign is taken when selecting the lower sideband.

Multiplying the complex signal spectrum $M(f)$, **Figure 1(b)**, by the transfer function of the sideband filter, **Equation (A4)**, inverse Fourier transforming, and amplitude scaling results in

$$2\cdot\mathcal{F}^{-1}\left\{M(f)\cdot\left(\frac{1\pm\mathrm{sgn}f}{2}\right)\right\}=2\cdot\mathcal{F}^{-1}\left\{\frac{M(f)\pm\mathrm{sgn}f\,M(f)}{2}\right\}$$
$$=m(t)\pm j\hat{m}(t) \qquad \hat{m}(t) \qquad \text{(A5)}$$

which applies the definition that $\hat{m}(t)$ is the Hilbert transform of $m(t)$ found **[15]** by applying

$$\mathcal{F}^{-1}\{\mathrm{sgn}f\,M(f)=j\hat{m}(t)\} \qquad \text{(A6)}$$

Finally, the frequency translation shown in **Figure 4** is accomplished by multiplying by the complex exponential with frequency f_c representing the carrier frequency

$$x_c(t)=\left(m(t)\pm j\hat{m}(t)\right)e^{j2\pi f_c t}. \qquad \text{(A7)}$$

For filtering at the carrier frequency, frequency translation shifts the double-sided spectrum to the carrier frequency

$$M(f-f_c) \qquad \text{(A8)}$$

expressed in a compact way the frequency shifted sideband filter transfer function, **Figure 6**, is

$$H(f-f_c)=\frac{1\pm\mathrm{sgn}(f-f_c)}{2} \qquad \text{(A9)}$$

where the convention introduced previously for sideband designation still applies.

Multiplying the frequency translated complex signal spectrum

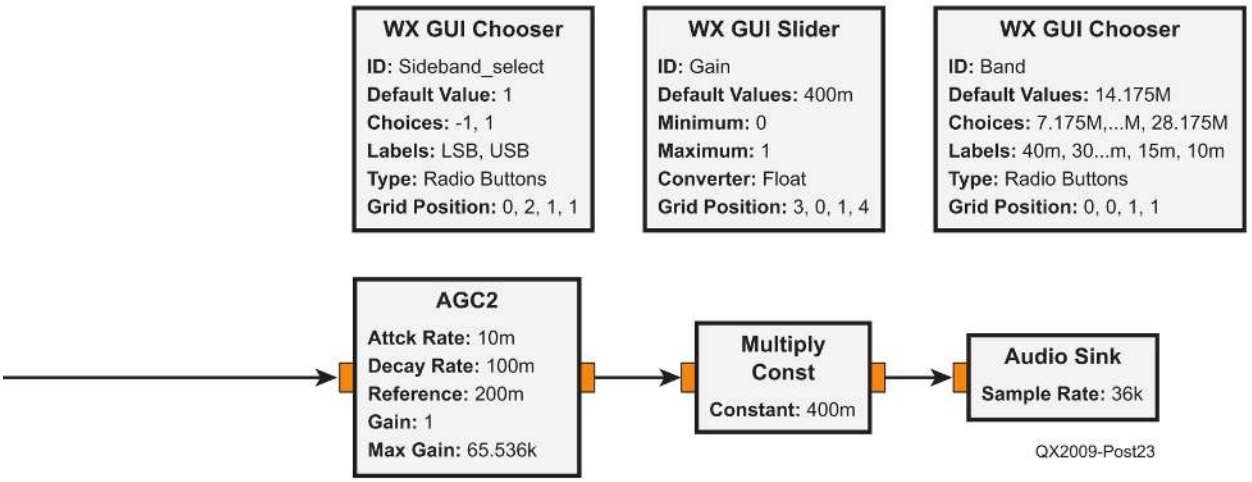

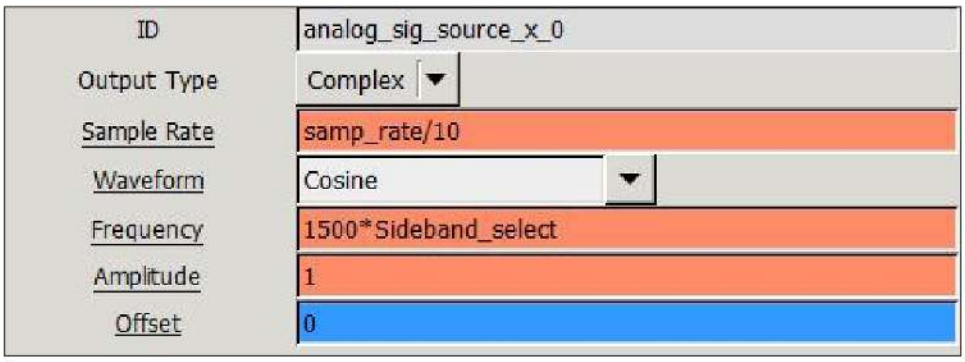

Figure 24 — Complex exponential source properties depicting method of offset frequency selection.

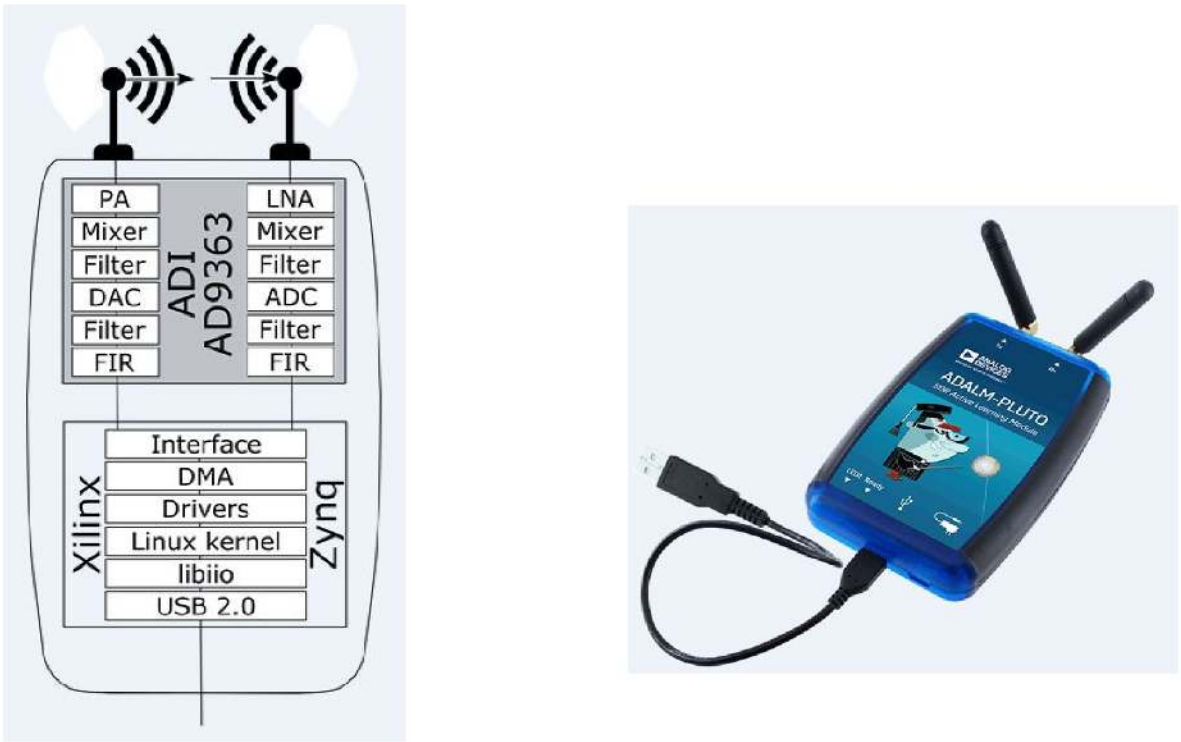

Figure 25 — PlutoSDR (left) block diagram and (right) photograph (Courtesy of Analog Devices).

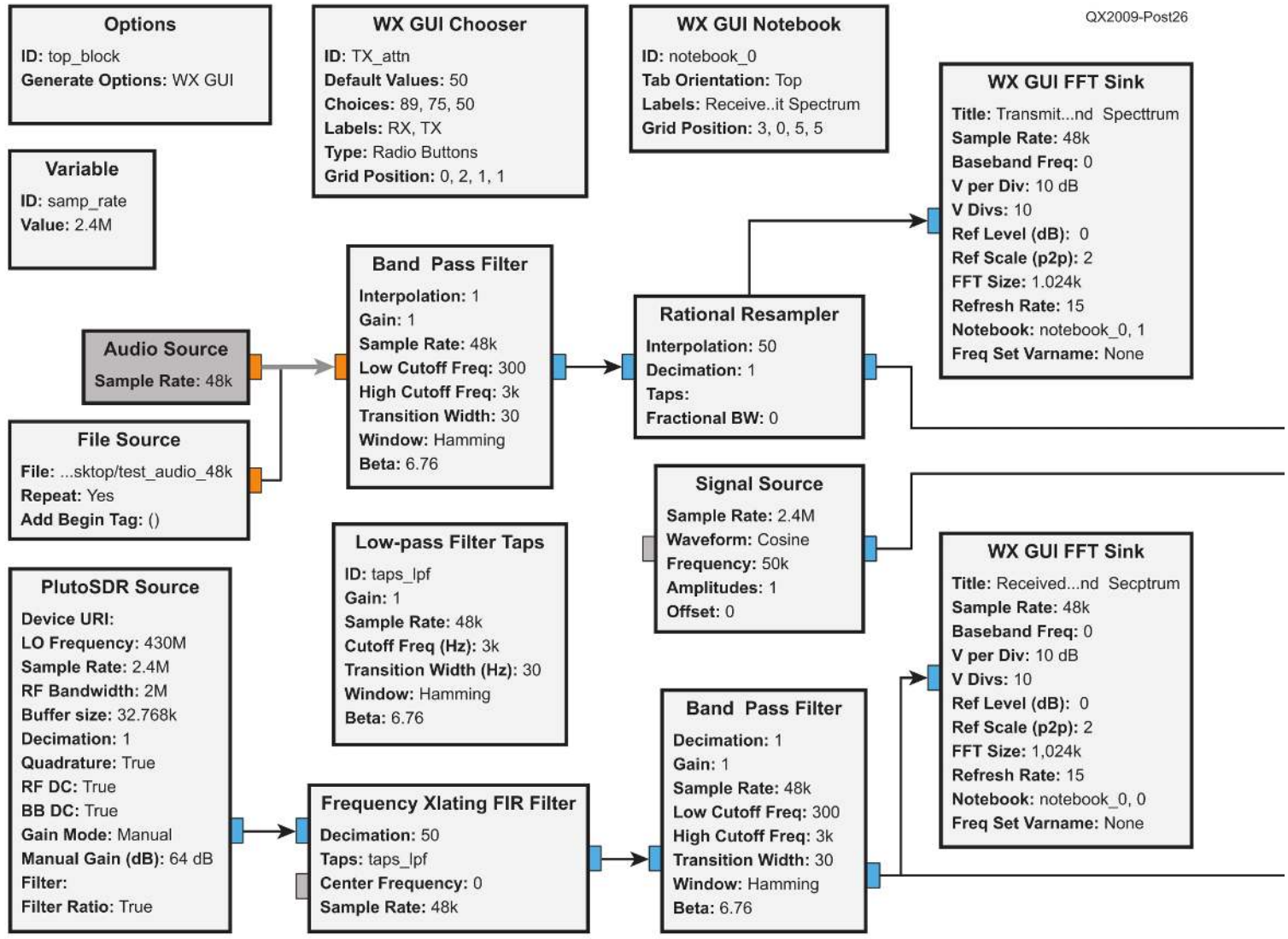

Figure 26 — *GRC* flowgraph for 70-cm SSB transceiver using an ADALM-Pluto SDR transceiver.

(A8) by the transfer function of the frequency shifted sideband filter **(A9)** results in

$$M\left(f-f_c\right)\cdot\left(\frac{1\pm\operatorname{sgn}\left(f-f_c\right)}{2}\right)$$
$$=\frac{M\left(f-f_c\right)\pm M\left(f-f_c\right)\operatorname{sgn}\left(f-f_c\right)}{2} \quad \text{(A10)}$$

Applying the definition of the Hilbert transform to **(A10)** inverse Fourier transforming, and then amplitude scaling gives

$$x_c\left(t\right)=2\mathcal{F}^{-1}\left\{\frac{M\left(f-f_c\right)\pm M\left(f-f_c\right)\operatorname{sgn}\left(f-f_c\right)}{2}\right\} \quad \text{(A11)}$$
$$=\left(m\left(t\right)\pm j\hat{m}\left(t\right)\right)e^{j2\pi f_c t}$$

which also applies the frequency-translation theorem

$$\mathcal{F}^{-1}\left\{M\left(f-f_c\right)\right\}=m\left(t\right)e^{j2\pi f_c t} \quad \text{(A12)}$$

and matches the result in **(A7)** shown above.

Appendix 2

The modulation theorem states that the multiplication of cosine or sine, with frequency f_o, and the message signal $m\left(t\right)$ can be expressed as

$$m\left(t\right)\cdot\cos\left(2\pi f_o t\right)=\mathcal{F}^{-1}\left\{\frac{1}{2}M\left(f-f_o\right)+\frac{1}{2}M\left(f+f_o\right)\right\} \quad \text{(A13)}$$

or

$$m\left(t\right)\cdot\sin\left(2\pi f_o t\right)=\mathcal{F}^{-1}\left\{\frac{1}{2j}M\left(f-f_o\right)-\frac{1}{2j}M\left(f+f_o\right)\right\}. \quad \text{(A14)}$$

The transfer function for a low-pass filter, with cutoff frequency $\pm f_o$, is

$$H\left(f\right)=\frac{1}{2}\operatorname{sgn}\left(f+f_o\right)-\frac{1}{2}\operatorname{sgn}\left(f-f_o\right). \quad \text{(A15)}$$

The output of the low pass filter on the upper branch, **Figure 15**, is the in-phase signal

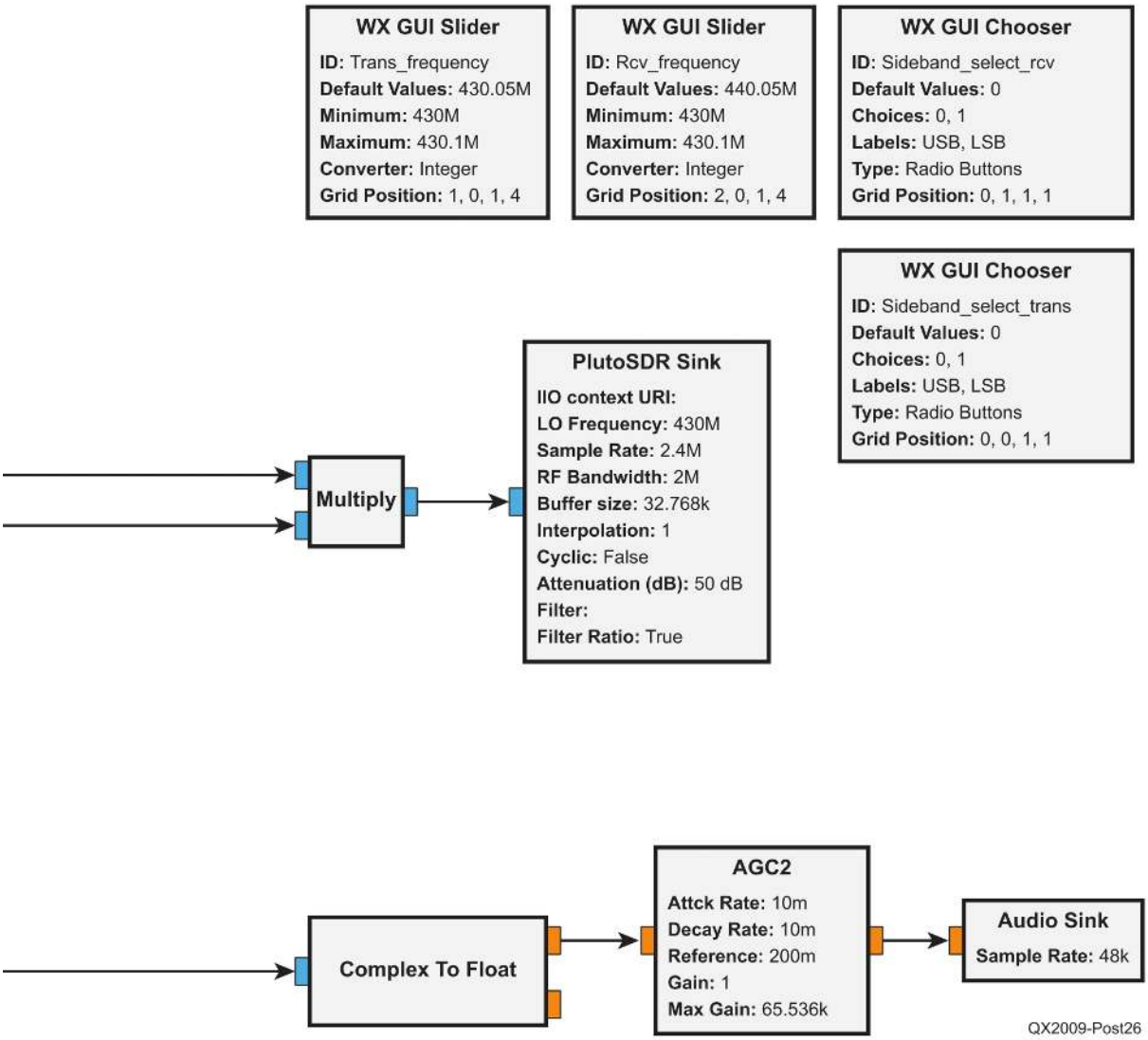

$$i(t)=\mathcal{F}^{-1}\left\{\begin{array}{l}\left(\frac{1}{2}M(f-f_o)+\frac{1}{2}M(f+f_o)\right)\\ \bullet\left(\frac{1}{2}\mathrm{sgn}(f+f_o)-\frac{1}{2}\mathrm{sgn}(f-f_o)\right)\end{array}\right\} \quad \text{(A16)}$$

which after multiplication and applying the result

$$M(f\pm f_o)\cdot\mathrm{sgn}(f\mp f_o)=\mp M(f\pm f_o)$$

becomes

$$i(t)=\mathcal{F}^{-1}\left\{\frac{1}{4}\begin{pmatrix}M(f-f_o)\\ -M(f-f_o)\mathrm{sgn}(f-f_o)\\ +M(f+f_o)\mathrm{sgn}(f+f_o)\\ +M(f+f_o)\end{pmatrix}\right\}. \quad \text{(A17)}$$

Applying the definition of the Hilbert transform and the frequency translation theorem to **(A17)** results in

$$i(t)=\frac{1}{4}m(t)\left(e^{j2\pi f_o t}+e^{-j2\pi f_o t}\right)+\frac{j}{4}\hat{m}(t)\left(e^{-j2\pi f_o t}-e^{j2\pi f_o t}\right). \quad \text{(A18)}$$

The output of the low-pass filter on the lower branch, **Figure 15**, is the quadrature signal

$$q(t)=\mathcal{F}^{-1}\left\{\begin{array}{l}\left(\frac{1}{2j}M(f-f_o)-\frac{1}{2j}M(f+f_o)\right)\\ \bullet\left(\frac{1}{2}\mathrm{sgn}(f+f_o)-\frac{1}{2}\mathrm{sgn}(f-f_o)\right)\end{array}\right\}, \quad \text{(A19)}$$

which after multiplication and applying the result

$$M(f\pm f_o)\cdot\mathrm{sgn}(f\mp f_o)=\mp M(f\pm f_o)$$

becomes

$$q(t)=\mathcal{F}^{-1}\left\{\frac{1}{4j}\begin{pmatrix}M(f-f_o)\\-M(f-f_o)\operatorname{sgn}(f-f_o)\\-M(f+f_o)\operatorname{sgn}(f+f_o)\\-M(f+f_o)\end{pmatrix}\right\}. \tag{A20}$$

Applying the definition of the Hilbert transform and the frequency translation theorem to **(A20)** results in

$$q(t)=\frac{1}{4j}m(t)\left(e^{j2\pi f_o t}-e^{-j2\pi f_o t}\right) - \frac{j}{4j}\hat{m}(t)\left(e^{j2\pi f_o t}+e^{-j2\pi f_o t}\right) \tag{A21}$$

Adding **(A18)** and **(A21)** in the form $2\left(i(t)\mp jq(t)\right)$, and multiplying by the complex exponential representing the carrier frequency results in

$$x_c(t)=\left(m(t)\pm j\hat{m}(t)\right)e^{j2\pi(f_c\mp f_o)t}. \tag{A22}$$

Based on Weaver's work**[5]**, a reasonable choice for f_o is $f_o=f_m/2$. With this substitution, **(A22)** becomes

$$x_c(t)=\left(m(t)\pm j\hat{m}(t)\right)e^{j2\pi\left(f_c\mp\frac{f_m}{2}\right)t}. \tag{A23}$$

John E. Post, KA5GSQ, is an associate professor of electrical engineering with Embry-Riddle Aeronautical University in Prescott, AZ. He was first licensed in 1976 and currently holds an Amateur Extra class license. John has BS, MS, and PhD degrees in electrical engineering.

References

[1]G. McElroy, "Amateur Radio and the Rise of SSB," *QST*, Jan. 2003, pp. 45–47.
[2]A. A. Oswald, "Early history of single-sideband transmission," *Proc. IRE*, Dec., 1956, pp. 1676–1679.
[3]P. H. Young, **Electronic communications techniques, 5th Ed.**, Pearson Prentice Hall, 2004.
[4]D. E. Norgaard, "The phase-shift method of single-sideband signal generation," *Proc. IRE*, Dec. 1956, pp. 1718–1735.
[5]D. K. Weaver, Jr., "A third method of generation and detection of single -sideband signals," *Proc. IRE*, Dec., 1956, pp. 1703–1705.
[6]**https://wiki.gnuradio.org/index.php/Main_Page**.
[7]**https://www.sdrplay.com/docs/gr-sdrplay-workflow.pdf**.
[8]**mercury.pr.erau.edu/~postj/signals/**.
[9]**www.sdrplay.com**.
[10]**www.analog.com/media/en/news-marketing-collateral/product-highlight/ADALM-PLUTO-Product-Highlight.pdf**.
[11]**www.analog.com/en/design-center/evaluation-hardware-and-software/evaluation-boards-kits/ADALM-PLUTO.html#eb-overview**.
[12]**https://wiki.analog.com/university/tools/pluto/users/customizing**.
[13]**www.aaronscher.com/wireless_com_SDR/Create_Live_USB_GNU_Radio.html**.
[14]**https://wiki.analog.com/resources/tools-software/linux-software/gnuradio**.
[15]R. E. Ziemer and W. H. Tranter, **Principles of Communications: Systems, Modulation and Noise, 6th Ed.**, John Wiley & Sons, 2009.

Gwyn Griffiths, G3ZIL
14 Bassett Close
Southampton SO16 7PE, UK;
gwyn@autonomousanalytics.com

Rob Robinett, AI6VN
357 Gravatt Drive
Berkeley, CA 94705, USA;
rob@robinett.us

Glenn Elmore, N6GN
7319 Silvermoon Lane
Fort Collins, CO 80525, USA;
n6gn@sonic.net

Estimating LF – HF Band Noise While Acquiring WSPR Spots

Systematic measurements of noise at your receiver can help improve your station performance and provide insights into the ionosphere and propagation.

Noise levels are a topic of long-standing concern to radio amateurs. Over recent years a perceived upward trend in noise levels has added to that concern. This has led to a number of initiatives by national amateur radio societies including in the UK **[1]**, the Netherlands **[2]**, South Africa **[3]** and Germany **[4]**, and ARRL have recently laid the groundwork for a noise study in a rural environment. Other spectrum users are also affected; for over 30 years the US Government has supported a *Signal-to-Noise Enhancement Program* to measure, identify and mitigate noise and interference. There is an example in the public domain of the methods used and results obtained during a 2010 investigation at a Department of Defense receiver facility at Key West, Florida **[5]**.

Our own motivation to measure noise came from our use of the Weak Signal Propagation Reporter (WSPR) mode. While WSPR reception records include an estimate of the signal to noise ratio (SNR) they do not include an estimate of the noise. Attempts at gleaning reliable information on, for example, the hour-by-hour or day-to-day changes in signal level for a particular path can be hampered by changes in the noise level. This was the challenge communicated to us by Larry Plummer, W6LVP, as part of his study of his propagation path to Danie Mans, ZS3D. It was also our expectation that systematic noise measurements would help us understand and then minimize the noise at our own locations and within our own receiving systems.

We were also keen to make measurements at a site with very low local noise levels that one of us (AI6VN) has access to. The Maritime Radio Historical Society (MRHS) preserves the ex-RCA coast radio receiving station KPH at Point Reyes, California **[6]**, a site chosen by Dr. Harold Beverage that began operations in 1929. We considered that this remote site, within the Point Reyes National Seashore, with proper care, could act as a reference station not subject to local noise or interference. This, indeed, proved to be the case.

Our approach has been to add two noise estimation algorithms to a script, *wsprdaemon*, a robust WSPR decoding and reporting program written by Robert Robinett, AI6VN **[7]**. Plots of noise from several stations on WSPR bands from 2200 m to 10 m are reported in real time at **wsprdaemon.org/graphs** and data are also publicly available from an Influx database via a Grafana web tool **[8]**.

In this article we outline the types of noise we are trying to measure, and those we are not, the time and frequency domain algorithms currently in use, and matters of calibration. We show examples of use, comparing noise and SNR for a ground wave signal, the daily pattern of noise at KPH, patterns of variation in noise at two receivers 1000 km apart, and the change in daily noise patterns with season. We close with a discussion on these results and how we intend to develop the noise-measuring capability within *wsprdaemon*.

Types of Noise We are Trying to Measure

At this stage of our study our noise measurements are intended to include the contributions from the following sources:

• *Galactic noise from the sun or other celestial sources*. For example, at a low noise location above 20 MHz one might expect to see noise variations from galactic sources in synchrony with a sidereal day (about 23 hours 56 minutes) when the sun is inactive.

• *Natural, atmospheric noise from global lightning (sferics)*. The result of global lightning has been likened to a "drizzle" of broadband noise, very different from the individual, identifiable crashes from local and regional thunderstorms. The local noise level from distant thunderstorms decreases with frequency and shows a diurnal variation with the lowest levels below about 10 MHz during the day, due to absorption in the lower ionosphere, with a significant increase at night.

• *Artificial noise from the myriad of electrical and electronic items of the modern world*. Compact sources are most likely to produce only a very local near-field impact, when their dimensions, or the lengths of wiring, are much smaller than the wavelength(s) of the unwanted emissions. Some equipment with power and or signal leads, without suppression, of a length approaching or exceeding quarter of a wavelength may radiate and have an impact over a wider area.

• *Common mode coupling is an avoidable ingress mechanism for noise*. Where it allows ingress of the types of noise listed above our objective has been to use these measurements as one of several tools to identify and then eliminate, *e.g.* appropriate use of baluns, including tuned baluns, grounding, elimination of current loops and, specifically for the KiwiSDR, using a WiFi connection rather than Ethernet.

Types of Noise We Do Not Want to Measure

Future work may be undertaken to

provide separate estimates of noise level and frequency of occurrence from these sources, but for now, our chosen measurement methods deliberately minimize their contribution to our noise estimates.

• *Noise from local thunderstorms.* While this type of noise is broadband it is intermittent, and hence can be excluded by selecting a time window when not present.

• *Artificial impulsive noise.* Even if this type of noise is repetitive, for example, arcing switch contacts, there will likely be times when it is not present.

• *Interference from radio signals.* There are times when amateur transmissions of CW or data modes such as RTTY or PSK31 occur in the bands used by WSPR. Continuous and sporadic carriers have also been seen. These types of signals can be excluded, even if continuous, by making our measurements within gaps in the frequency spectrum.

Despite the good degree of clarity in these intentions for the types of noise we do and do not seek to measure much remains unknown. We have imperfect understanding of the incoming and local sources of noise and of the coupling mechanisms. There are, therefore, limitations to the measurements described here, but as we show through several examples, they do provide useful insights and ideas for further investigation.

Appropriate Noise Measurement Methods

From the requirements outlined above of what noise we do and do not want to measure, two general approaches emerge. First, measure the minimum true RMS level over one or more short, fixed-width windows that are allowed to occur anywhere within a longer time window. Second, over a specified overall time window measure the spectral components over an appropriate bandwidth in a number of short time windows and take a fraction of the total number of spectral estimates, irrespective of frequency or time, that form the lowest *x%* of the values. We've called these our RMS and FFT methods respectively.

The following sections illustrate these two methods in more detail as we have applied them to estimating noise concurrent with the reception of WSPR signals. For both methods, to minimize programming effort, we have used the cross-platform *Sound eXchange* (*SoX*) software package **[9]**. Specifically, we use *SoX's* trim and stats options to set the time window and calculate a trough value for the RMS method, and the stat -freq option for the FFT method.

Both methods are applied to the same audio capture file in *wav* format obtained from a receiver. For the work reported here the audio capture is done by the program *wsprdaemon* that also decodes and reports WSPR spots **[7]**. Options are provided for analog baseband audio via a sound card, or network audio from an RTL or other SDR using the *Soapy* remote protocol, or as used for the measurements in this paper, via a network connection to a KiwiSDR using the *kiwirecorder.py* utility **[10]**. A diagram that outlines our noise measurement system and these options is shown in **Figure 1**.

The RMS Method Applied to WSPR

WSPR transmissions start one second past each even minute and end at about 111 seconds. This schedule, in theory, provides a gap of one second before, and eight seconds after a transmission. Of course, in practice a transmission may start early or finish late. We chose to use 0.25 – 0.75 s and 113 – 118 s as the overall pre- and post- transmission time windows, but they can be altered. The *SoX* stats option calculates the lowest RMS level over a 50 ms window within the set interval.

Figure 2 shows histograms of uncalibrated noise level obtained using the RMS method over a set of 405 two-minute WSPR intervals between 7039.94 kHz and 7040.26 kHz on 14 – 15 March 2019 at G3ZIL, Southampton, UK. The three histograms are for the pre- and post-transmission intervals, and for the minimum of the two in each interval. To the right of each histogram outliers are shown as dots, the box being the central distribution, and the quantiles between 25% and 100% are listed. At each quantile the noise level estimate from the post-transmission period is lower than for pre-transmission. This is an expected result as the post-transmission time window is longer, allowing a greater margin for a mistimed transmission. Taking the minimum of the pre- and post-transmission estimates results in fewer outliers. Therefore, while we will see outlier estimates of noise when using this method, they can easily be removed, if required, by post-processing the data using a median filter.

The FFT Method Applied to WSPR

The *SoX* stat -freq option automatically splits an input audio file into time segments appropriate to a 4096-point FFT, providing 2048 Fourier coefficients for the positive half-space. Given the 12000 Hz sample rate and the two-minute duration of the baseband *wav* file produced by *kiwirecorder.py* this results in 352 blocks of Fourier estimates. Our analysis covers the band from 1338.98 Hz to 1661.27 Hz, which for convenience we refer to as 1340 – 1660 Hz. This is sufficient to cover the WSPR band of 1400 – 1600 Hz and matches the band-pass set in the *kiwirecorder.py* option list. We illustrate our method using a single *wav* file recorded at KPH, Point Reyes, California at a WSPR dial frequency of 7038.6 kHz at 1116 UTC on 19 April 2019.

Figure 3A shows the spectrum from 1340 – 1660 Hz where the power in each 2.9 Hz band in each of the 352 blocks has been summed. From the LF end the SNRs reported by WSPR for the three high peaks were –9, –7 and –7 dB. The three lower, but distinct, peaks at 1431, 1557 and 1574 Hz were also decoded with SNRs of –27, –28 and –23 dB. The signal with an observable peak at 1450 Hz was not decoded. In **Figure 3B** the individual spectrum power estimates are plotted in ascending order (this is not

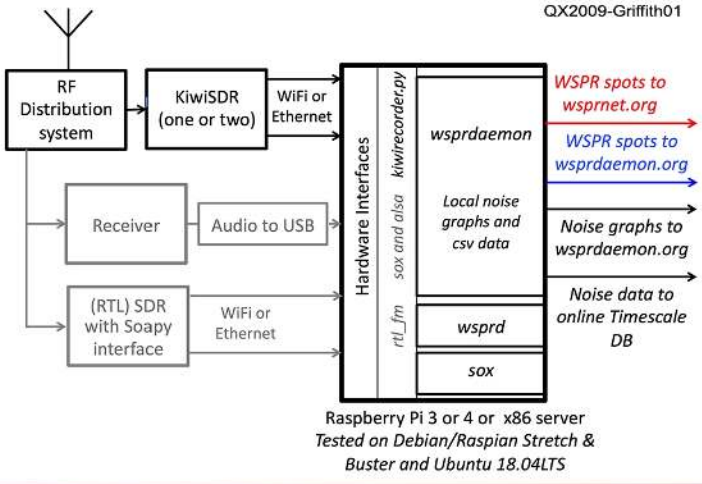

Figure 1 — Block diagram of the noise measurement arrangement. Software modules are in italics. While *wsprdaemon* and its noise measurement can use an audio input or an RTL-SDR via a *Soapy* interface, they are greyed out because they were not used for the examples in this article.

a cumulative graph), and a dashed line is shown at 30% of the entire spectrum. In this case 30% represents 33 frequency bins out of the full set of 111. While our decision to consider the sum of the power spectrum to this 30% point, and to use that bandwidth (97 Hz) as the basis to derive the noise level in 1 Hz, is to some degree arbitrary. There are three reasons for this choice. First, it is well above the region with higher slope below about 15%. Second, it is well below the start of another upward slope above 60%. Third, it is less than 37% that represents the ratio of our guard band of ±60 Hz either side of the 200 Hz WSPR band. One hypothesis for the rise above 60% is that it represents the sum of the power from WSPR signals that are, individually, below the decode threshold of about –30 dB SNR in a 2.5 kHz bandwidth.

Over a set of 33 two-minute WSPR intervals recorded at KPH at the WSPR dial frequency of 7038.6 kHz on 19 April, the histogram in **Figure 4** illustrates the number of times spectral bands (here in 10 Hz groups) were within the lower 30%. Preferentially, but not exclusively, the algorithm used noise power estimates within the 60 Hz guard bands above or below the 1400 – 1600 Hz WSPR band; 30.4% being

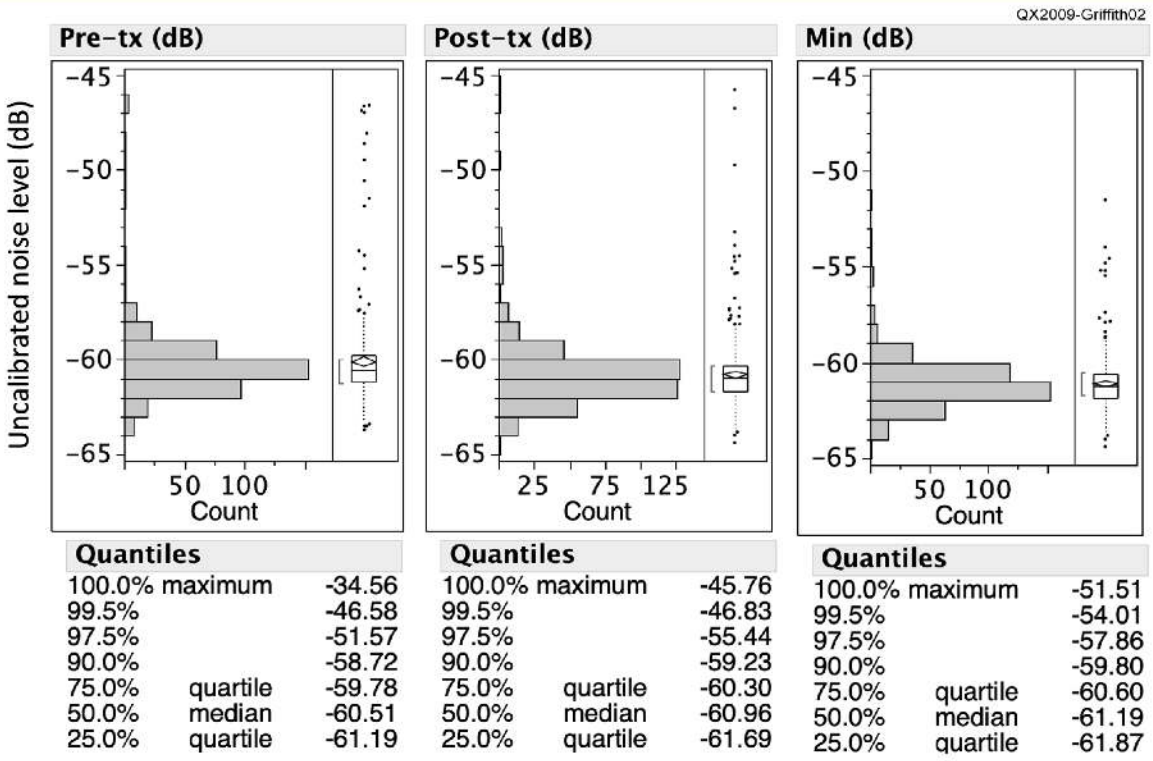

Quantiles		
100.0% maximum		-34.56
99.5%		-46.58
97.5%		-51.57
90.0%		-58.72
75.0%	quartile	-59.78
50.0%	median	-60.51
25.0%	quartile	-61.19

Quantiles		
100.0% maximum		-45.76
99.5%		-46.83
97.5%		-55.44
90.0%		-59.23
75.0%	quartile	-60.30
50.0%	median	-60.96
25.0%	quartile	-61.69

Quantiles		
100.0% maximum		-51.51
99.5%		-54.01
97.5%		-57.86
90.0%		-59.80
75.0%	quartile	-60.60
50.0%	median	-61.19
25.0%	quartile	-61.87

Figure 2 — Histograms of uncalibrated noise level from *SoX* stats RMS 50 ms trough measurements pre- and post-transmission, and the minimum of these minima for 405 two-minute WSPR intervals between 7039.94 kHz and 7040.26kHz on 14 – 15 March 2019 at G3ZIL, Southampton, UK.

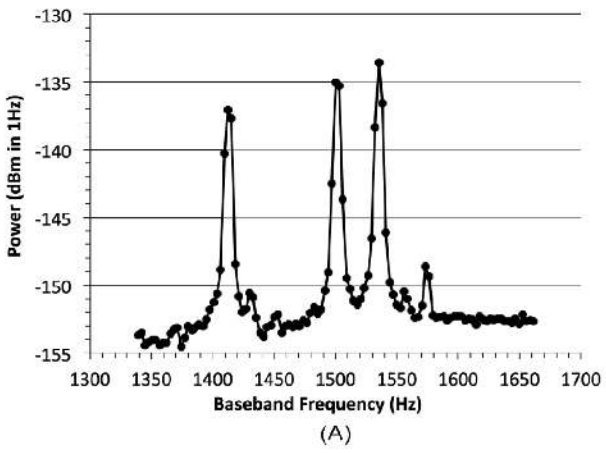

Figure 3A — Baseband power spectrum from a single two-minute *wav* file recorded at KPH, Point Reyes, California with a WSPR dial frequency of 7038.6 kHz at 1116 UTC on 19 April 2019 showing three strong and four weak WSPR signals.

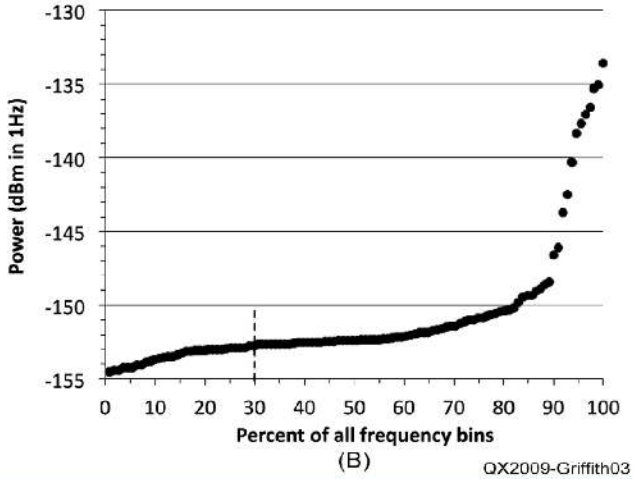

Figure 3B — Power spectrum estimates as in Figure 3A but sorted in ascending order. Our noise estimate is based on the sum of the noise power in the lower 30%.

below 1400 Hz, 26.5% being above 1600 Hz and 43.1% within the WSPR band, representing 0.55, 0.44 and 0.21% per Hz respectively. While the detailed distribution changes from hour to hour we have found that the broad characteristic shape of the histogram remains stable.

This method is similar to, but not exactly the same, as that used within the WSPR decoder. Within the WSPR decoder (*wsprd*) the noise is estimated over ±150 Hz, *i.e.* from 1350 – 1650 Hz, averaging by frequency the amplitude in 512-point FFTs, applying a 7-point rectangular window filter, sorting the resulting coefficients by amplitude and taking the single coefficient at the 30th percentile as the noise level.

Calibration

At this stage of the project, our primary aim is to report noise levels at the antenna socket of the receiver in units of dBm in 1 Hz using a well-understood calibration over the full amplitude and frequency range. The practical details of the calibration methods will depend to some extent on the type of receiver used, in particular whether analogue or SDR, and how signal level measurements can be made. We have described in detail our measurement approach for the KiwiSDR in a technical report available on-line **[11]**. The following are the key points relevant to the examples described in this article.

Despite the KiwiSDR being a direct sampling receiver the gain is not constant over the range 10 kHz to 30 MHz. In summary, the deviation from a flat response is –2 dB at 10 kHz and a broad peak between 12 MHz and 30 MHz with a maximum of +3 dB at 21 MHz. This response is broadly consistent between units and is not due to the theoretical or measured transfer function of the 7-pole Chebyshev low pass filter. Consequently, the *wsprdaemon* script provides a default amplitude correction for each WSPR band, which the user can adjust.

The *wsprdaemon* noise measurements are made in a commanded 320 Hz bandwidth, but reported in a 1 Hz bandwidth. As the shoulders of the KiwiSDR digital filters intrude (asymmetrically) into the commanded passband the calculated equivalent noise bandwidth is used to convert the measurements in the nominal 320 Hz passband to 1 Hz.

Using a fixed gain rather than AGC and a 16-bit *wav* file as the audio source restricts the dynamic range. Through empirical tests we arrived at a fixed gain setting that results in the receiver self-noise exercising 3 – 5 bits while providing sufficient dynamic range such that clipping typically occurred only during 1 in 200 two-minute intervals at KPH.

As the KiwiSDR does not use front-end band-pass filters the user must be sure that the sum total of all signals does not cause overload, *wsprdaemon* now logs any instances of overload to help interpret biased noise level estimates. However, non-linearity and imperfect alias rejection can result in a higher noise level within the measurement band due to strong, but below overload, out-of-band signals. We have made measurements of the Noise Power Ratio using both single tone and broadband noise, which suggests that at an input level of –15 dBm (just below overload) the additional noise is about –158 dBm in 1 Hz.

Finally, there are questions of definition and robustness for the noise estimate. While the methods to obtain the RMS and FFT estimators are based on well-defined algorithms, both lack robustness in the presence of some types of noise, which inevitably bias a measurement high. The choice of "best" estimator for the background noise level has been studied extensively within the long-running US Government *Signal-to-Noise Enhancement Program* **[12]**. Their preferred estimator is based on a kernel smoothing model fit (KSnf) to the first peak of a histogram of frequency of occurrence against binned median received power per frequency bin. For the example distribution shown in **Figure 4** the difference between our 30% quantile FFT estimator and the KSnf method is very small at 0.1 dB (–152.7 dB and –152.6 dB respectively), but undoubtedly the difference will depend on the characteristics of the noise.

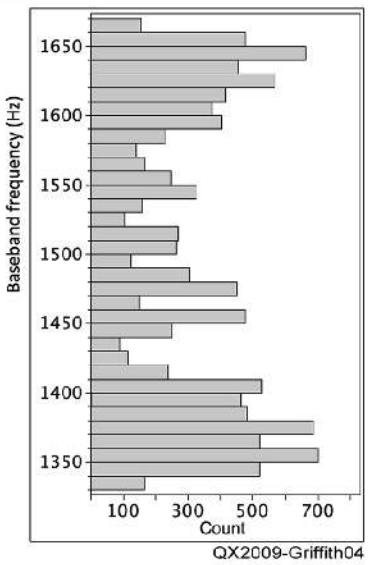

Figure 4 — An example histogram in 10 Hz bands of the frequency bins forming the lowest 30% with lowest power coefficients, comprising data gathered over 33 two-minute intervals at KPH on 19 April 2019 at a WSPR dial frequency of 7038.6 kHz.

Comparison of Our Noise Estimates with the WSPR SNR for a Ground Wave Signal

One approach to validating our noise estimates is by assuming that the received level of a ground wave signal remains constant, and that changes in the estimated SNR of the signal are from changes in noise rather than the signal. We consider this a reasonable assumption if ground conductivity is constant and there is no reception via the ionosphere during an experiment. WSPR transmissions on 40 m from a QRP Labs U3S at N2AJX using an AS-2259 turnstile inverted **V** antenna modified for 80 and 40 m **[13]** were received 20 km distant on a Beverage antenna at KD2OM with a KiwiSDR and *wsprdaemon* software.

Figure 5A shows scatter plots of the RMS and **Figure 5B** shows FFT noise estimates, and the 1 dB quantized WSPR SNR for each 2-minute interval when a WSPR spot was received. The noise estimates have been adjusted to a bandwidth of 2.5 kHz to match how the WSPR SNR is reported. Of course, the actual WSPR SNR is about 32 dB higher, given that the signal processing bandwidth for each tone is about 1.5 Hz and not 2.5 kHz. Also shown are non-parametric density contours from 10% (outer) to 90% (inner); these contours aid our interpretation of these scatter plots. Also shown is a 1:1 line representing the hypothesis that, for S constant, changes in SNR should have an inverse 1:1 relationship with changes in N. Therefore, we would expect the scatter plots to show a slope parallel to this line.

Visually, the FFT estimator comes closer to the expected form, although with a tendency to show a lower noise than implied by the SNR as the SNR decreases. That is, while the ridge of the non-parametric density contours is below, but close to, the line at an SNR of –3 dB the ridge is successively further below the line as SNR decreases. The RMS estimates are consistently below the line and, from the trend of the density contours, have a shallower slope. From our wider observations of noise on the LF to HF bands using these two methods it is clear that characteristics of the noise do affect each algorithm differently. By characteristics we mean that the noise may not be additive Gaussian white noise. For the examples in **Figure 5A** and **5B** the implication is that

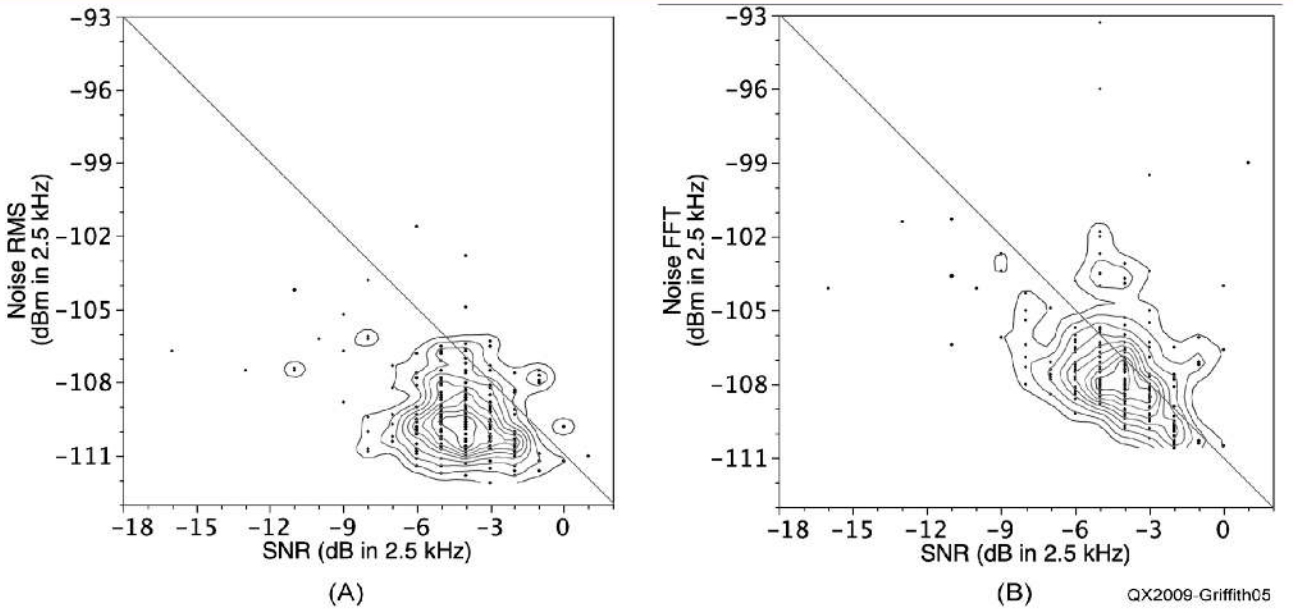

Figure 5 — Scatter plots of the RMS (A) and FFT (B) noise estimates against the 1 dB quantized WSPR SNR for each 2-minute interval. The observations were made between 5 November 2019 0000UTC and 7 November 2019 1156UTC, a total of 235 spots. The sloping line represents the hypothesized inverse 1:1 relationship between SNR and N if S is constant.

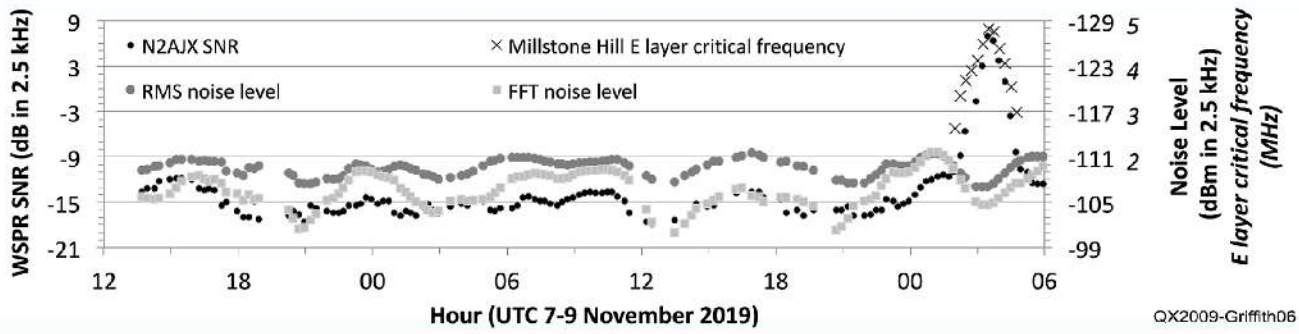

Figure 6 — Time series of the SNR of N2AJX WSPR transmissions received at KD2OM together with the noise level estimated by the RMS and FFT algorithms and the E layer critical frequency for 9 November. The data have been filtered using a running mean over one hour.

the RMS algorithm consistently found 50 ms periods when the noise was substantially less than from the FFT estimator over the lower 30% of frequency bins. Bursts of broadband noise would, as one example, be compatible with this observed difference. Given that the WSPR SNR estimate was derived using a binned FFT approach one would expect the SNR to show a closer relationship to our FFT method than to the RMS when the estimates from the FFT and RMS algorithms differed.

Times of convergence and divergence in the RMS and FFT noise estimates can be seen in the 42-hour time series in **Figure 6**. The data are from N2AJX ground wave signals received at KD2OM with N2AJX using a clone of a five-band CH250B 80 – 10 m vertical antenna and where one-hour moving average filters have been applied to the data. Near 0000 UTC (~1700 local time) on both days the two noise estimates, RMS in dark grey and FFT in light grey converged, yet at other times they differed by up to 6 dB. As yet, we do not have an explanation for this pattern of convergence and divergence.

Noting the reverse order secondary *y*-axis of **Figure 6** there are times of clear visual correlation between the SNR and both the RMS and FFT estimators of noise, for example from 1100 UTC on 8 November to 0100 UTC on 9 November. An analysis of the data between 1314 UTC on 7 November and 0114 UTC on 9 November gave a correlation coefficient of –0.60 for SNR and FFT, and –0.66 for SNR and RMS, both inverse correlations being statistically significant. For comparison, the correlation between the RMS and FFT noise estimators was +0.73. The correlation coefficient squared is an estimate of the proportion of the total variance explained by the independent variable. Here the correlation coefficient squared show 36% and 43% of the SNR variance to be explained by the RMS and FFT noise estimators — certainly an important factor, but suggesting the assumption of the variations of SNR only being due to variations in noise was an oversimplification.

Our correlation analysis between SNR and noise ended at 0114 UTC on 9 November because of the onset of ionospheric propagation. An ionosonde record for that time from the Millstone Hill Observatory, Massachusetts, about 500 km east of KD2OM, showed a sporadic E layer at 100 km height beginning to develop at 0130 UTC, persisting until 0515 UTC; the one-hour filtered E layer critical frequency f0Es from Millstone Hill is shown in **Figure 6 [14]**. During this interval of Es

propagation N2AJX SNR rose 19 dB to peak at +7 dB from a baseline of about −12 dB. At the same time the noise increased by about 5 dB from both RMS and FFT algorithms. The implication is that the true signal level rose by 24 dB and not 19 dB. One possible explanation for the observed change in noise, assuming it was dominated by distant, propagated-in noise, is from the large difference in the reception distance annulus at KD2OM between prior to and during the Es event. Characterizing the reception annulus by its lower quartile, median and upper quartile, the change was from 1661 – 5493 – 5922 km between 0000 – 0100 UTC prior to the event compared with 464 – 725 – 1798 km between 0300 – 0400 UTC during the Es peak.

Daily Patterns of Noise on 40 m and 60 m at KPH

Few amateurs are lucky enough to live in areas with such a low level of local noise as at KPH, Point Reyes, California. However, arriving at an RF distribution system and a receiver installation that matched the site's low level of noise was not immediate or straightforward. A Clifton/DX Engineering 23 dB preamplifier was installed after an 8-way splitter, a NooElec Distill AM broadcast band band-stop filter and a 30 MHz low-pass filter. Low-noise 1 MHz switched-mode power supplies are used, with Mini-Circuits T1-1 isolation transformers at the KiwiSDR inputs. At 7 MHz the noise floor of the KiwiSDR is −154 dBm in 1 Hz, equal to −120 dBm in 2.5 kHz, about S-1 (given 50 μV for S-9 and 6 dB per S-unit). **Figure 7** shows that the minimum received noise level at the antenna socket from the TCI530 log-periodic antenna, via the RF distribution system was about −147 dBm in 1 Hz, 9 dB above the receiver noise floor. Note that the TCI530 is not an isotropic antenna: differences in angle of arrival will alter the received levels.

There is a clear daily pattern to the noise. The sharply defined minimum occurred consistently at around 2000 UTC, that is, at noon local time. There was more variability in timing and in level for the peak, but over a ten-day period the highest peak was around 1900 local time followed by, on average, a plateau until 0600 local time, but with significant day-to-day variation including, on some days, a second peak. This observed diurnal noise level is consistent with rising absorption in the D layer from local sunrise, peaking at local noon then decaying by local sunset, with refraction from the merged F layers persisting, but decaying, due to the slow recombination of free electrons and ions.

While the RMS and FFT noise estimates in **Figure 7** are highly correlated (correlation coefficient of 0.87 with 1353 samples) and with a similar span (standard deviation of 6.0 dB for the RMS and 6.5 dB for the FFT) there is a clear offset, with the median of the FFT noise estimates 3.3 dB greater than for the RMS. In addition, in this example, the short-term variability of the RMS estimator is significantly less than for the FFT. However, we have found that offsets and differences in short-term variability are not always present, or if present, have the opposite trend between RMS and FFT than seen in this example **[15]**.

As we proposed that the explanation for the diurnal noise pattern in **Figure 7** was due to the diurnal pattern of propagation we have to show that the noise estimates are not being biased by higher signal levels between sunset and sunrise. To that end, **Figure 8** shows one 24-hour period 23 – 24 May 2019 at KPH for the 40 m and 60 m EU WSPR bands for the RMS noise estimator with local time. The broad pattern of the noise is the same for the two bands, with the minimum lower on 60 m than on 40 m, consistent with greater D layer absorption at the lower frequency.

WSPR spot counts per hour are shown using the right-hand axis in **Figure 8**. While the profile for the 40 m noise estimate does broadly follow the number of WSPR spots per hour, this is not the case for the 60 m EU segment. Only two transmissions were received during 2000 – 2059 and one between 2100 – 2159. Our conclusion is that the noise estimates were not due to bias from the WSPR signals, despite the visual correlation in **Figure 7** for 40 m; the noise was propagated-in from a multitude of different, distant sources.

Noise Pattern Variations at Two Receivers 1000 km Apart

Having looked at the daily pattern of noise at a single receiver, we now compare the pattern of noise variations at KPH (CM88mc) and KA7OEI in Northern Utah (DN31uo), about 1000 km apart on an approximately east-west path. Both use KiwiSDR receivers and TCI530 antennas, but differ in the splitters, filters and amplifiers between the antenna and the receiver. Hence offsets between noise level estimates at different sites are expected. However, those

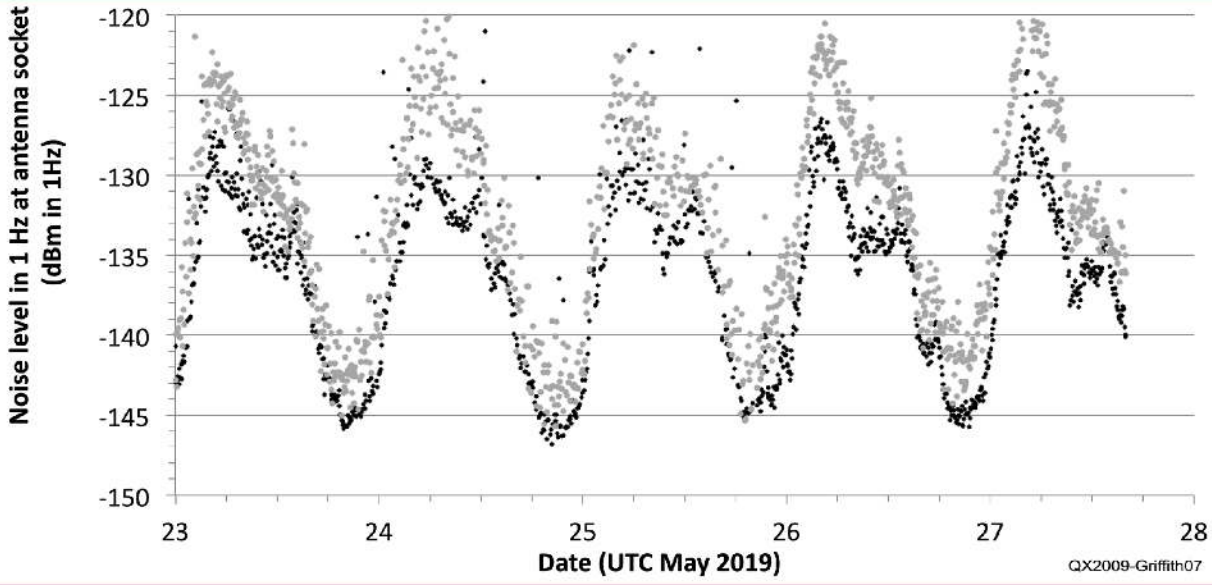

Figure 7 — Time series of the noise level recorded using a KiwiSDR at KPH, Point Reyes, California on 23-27 May 2019 using the RMS algorithm (black) and the FFT algorithm (grey) showing a clear, diurnal pattern, repeatable in the essential features of the time of minimum, and two peaks at the maximum.

offsets do not detract from the usefulness of the measurements for studying patterns in the noise.

An example time series for the FFT noise estimator over four days on the 80 m WSPR band (dial frequency 3.5686 MHz) for KPH and KA7OEI is shown in **Figure 9**. A 10-minute running mean filter has been applied to the 2-minute data. There are several points to note.

• At this time the noise floor at KA7OEI was higher by at least 12 dB than at KPH, seen as a plateau from about 1400 – 0000 UTC each day at KA7OEI without the round-bottomed dip seen at KPH **[16]**, 12 dB being the difference at the KPH minimum after the overall level reported by KA7OEI was adjusted so that the peaks coincided with those at KPH.

• Diurnal variations were dominant; with the late afternoon (local time) rise in noise level occurring consistently earlier at KA7OEI than at KPH. This is consistent with KA7OEI being east and north of KPH, sunset at KA7OEI on 1 September was 39 minutes ahead of KPH **[17]**. Prior to a cross-correlation analysis at 2-minute intervals spanning ±60 minutes a sixth order Butterworth low-pass filter with a cut-off period of eight hours was applied to both time series. This filter removed potential bias from shorter-period variations that may have different cross-correlation properties. The graph of correlation coefficient against lag / lead in **Figure 10** shows a broad peak centered at a lead of 38 minutes for KA7OEI (R = 0.939 compared with 0.924 at zero), in keeping with the expected time difference.

• Between 0230 and 1100 UTC each day, when D layer absorption was absent, there were variations in the noise, over periods of hours, which showed a similar form at the two receivers. Taking the data on 31 August and 3 September as examples, after applying cascaded low pass and high pass sixth order Butterworth digital filters to pass variations with periods between two and eight hours, results in the correlation coefficient profiles shown in **Figure 10**. The peaks were at zero lead on 31 August and at two minutes lead on 3 September. The implication being that variations with periods between two and eight hours occurred simultaneously at the two sites, 1000 km apart.

• Between 0600 – 0630 UTC on 2 September the noise level at KA7OEI dropped precipitously by 6 dB. This drop was followed by a train of cycles with a similar peak-to-peak magnitude and a period of the order of one hour. While a 6 dB precipitous drop in noise level was seen at KPH it occurred two hours thirty eight minutes after that at KA7OEI, and it was not followed by an obvious wave train. We currently have no sure explanation for these observations, although we suspect they may

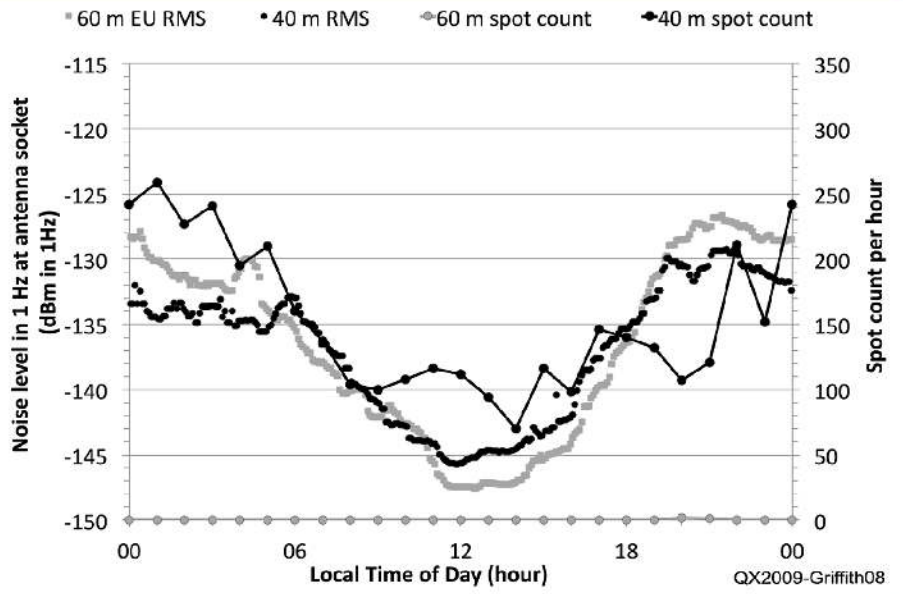

Figure 8 — A 24-hour time series of the noise level at KPH on 23-24 May 2019 using the RMS algorithm with local time of day for the 40 m and 60 m WSPR bands (dial frequencies of 7038.6 and 5364.7 kHz). The number of WSPR spots received in each hour is also shown, while the spot count for 40 m has the same overall pattern as the 40 m noise level only three spots were decoded on 60 m, showing that it is not the WSPR signals biasing the noise measurements.

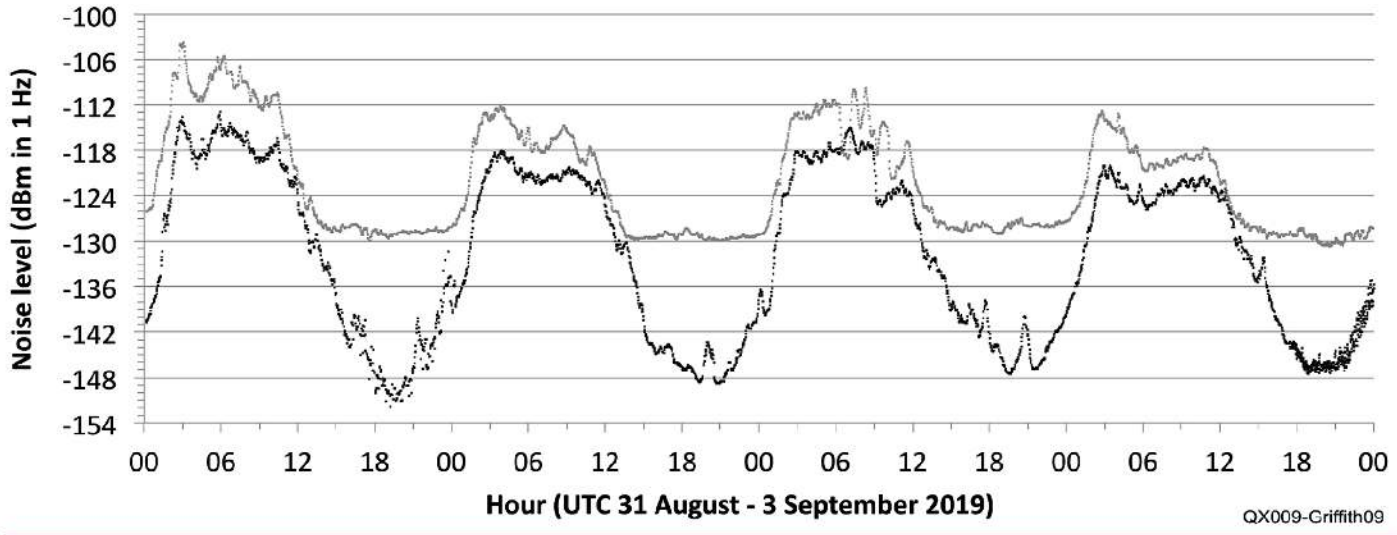

Figure 9 — Time series for the FFT noise level estimator on the 80 m WSPR band for KPH (black) and KA7OEI (grey) at a separation of about 1000 km for 31 August to 3 September 2019.

be associated with traveling ionospheric disturbances.

Changes in the Diurnal Pattern of Noise with Season

Seasonal changes in the diurnal pattern of noise on a single band can be illustrated using a shaded surface graphic with time of day on the *y*-axis, day of the year on the *x*-axis with the shading representing the noise level. **Figure 11** spans 12 June to 7 November for the 40 m WSPR band at OE9GHV, a quiet rural location near Alberschwende, Austria. The RMS algorithm noise estimates over two minutes were averaged into twenty-minute intervals, hence there are 72 points on the *y*-axis each day. The dark spots or rectangles are times when the KiwiSDR receiver was disconnected from the 80 m vertical loop antenna. These points therefore represent the noise level of the receiver itself. Black lines show the times in UTC of local sunrise and sunset.

During the summer, a prominent noise peak occurred consistently around sunset, with a weaker peak just after sunrise. The noise was at a minimum during daylight hours. However, after around day 264 (21 September, the autumn equinox) there was a gradual change, over about three weeks, from peak noise around sunset to a broader noise plateau starting just after sunrise and persisting until just before sunset. After this gradual change, the minimum noise occurred between sunset and sunrise.

Our working hypothesis for the springtime diurnal pattern at KPH (**Figures 7** and **8**) centered on D layer absorption causing the minimum noise during daylight hours, we suggest that it is also the cause of the observed summer daytime noise minimum. However, we do not have a hypothesis for the change in daily pattern in September, but we do know that there were no changes to the equipment or the local environment during that time. Despite an extensive literature search we have not found published results showing HF band noise in Europe by time of day and by season to provide a comparison or insights.

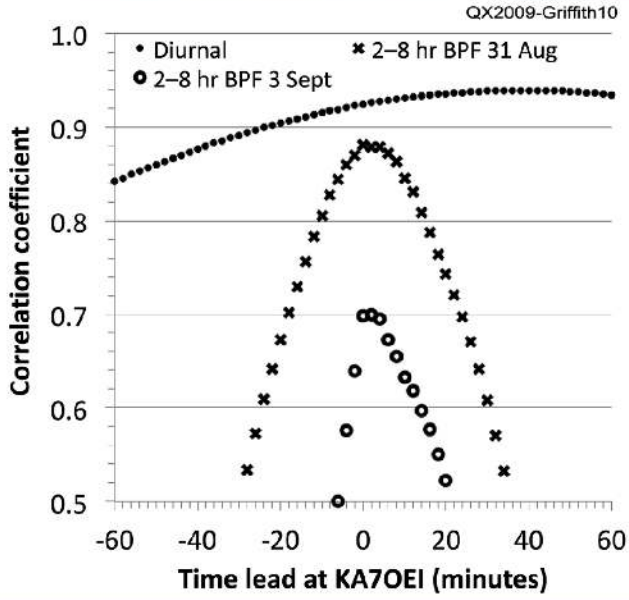

Figure 10 — Cross correlation coefficient between the noise level times series at KPH and KA7OEI shown in Figure 9 against lead time for the diurnal variation (periods over 8 hours) and for variations with periods between two and eight hours.

Discussion

The noise measurement capability within the *wsprdaemon* software is proving useful to a number of KiwiSDRs users in several

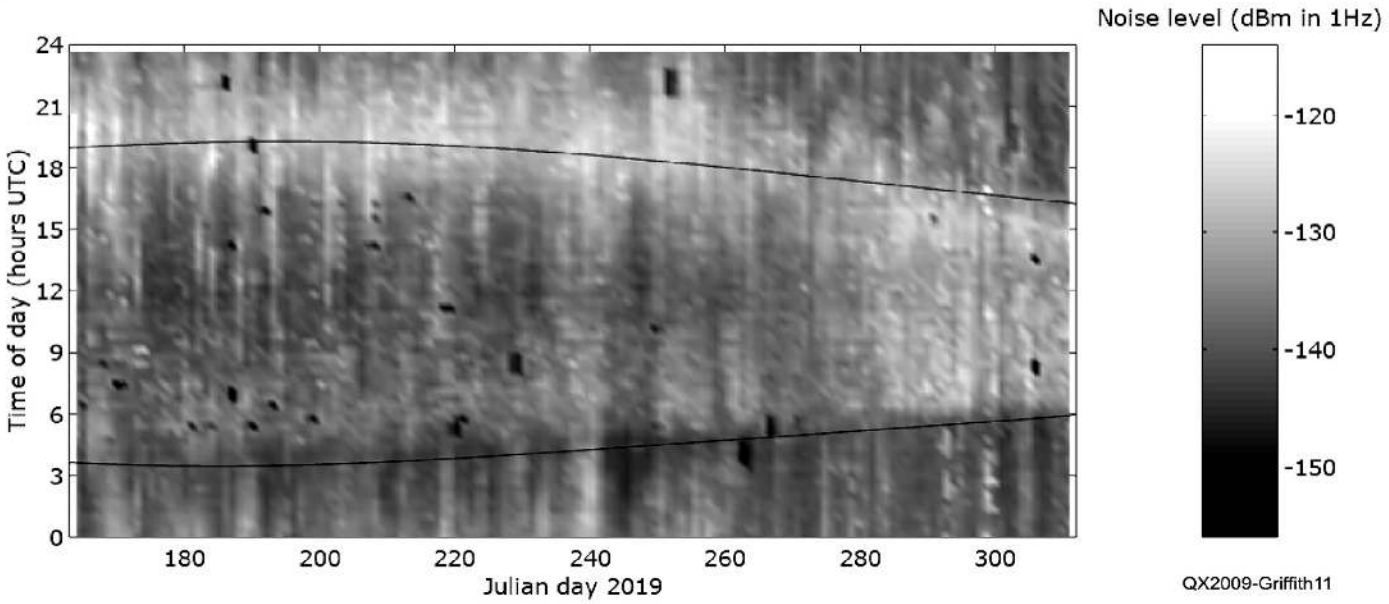

Figure 11 — Seasonal change in the pattern of diurnal noise on 40 m at OE9GHV, a quiet rural hilltop location near Alberschwende, Austria (JN47wk) from 12 June to 7 November 2019 together with lines at sunrise and sunset. After around day 264 (21 September, the autumn equinox) there is a change over about three weeks from peak noise slightly after sunset to a broader noise plateau starting just after sunrise persisting until just before sunset. The receiver is a KiwiSDR and the antenna an 80 m vertical loop via a splitter.

countries. While the two current estimators, a short-term RMS measurement in the time domain and a simple FFT and threshold approach in the frequency domain, have their limitations they do provide the basis for further analysis as shown by the examples in this article. We have started to experiment with adding a Kernel Smoothing model-fitting algorithm to the FFT data, both to evaluate its performance and the additional computational load.

Estimating noise level at the antenna socket of the receiver was the initial goal of this work, and it remains the best-controlled reference point as regards noise level calibration with frequency and receiver settings. However, *wsprdaemon* does provide a simple means in a configuration file for the user to set a band-by-band correction. To date, users that have applied these corrections have done so to account for gain or loss in their distribution system from the antenna. In these cases, the reference point moves to the antenna terminals. In either case, the noise measurement includes noise that may come from common mode coupling into the antenna cabling or from the power supplies of preamplifiers for example. This is very much a practical measurement, of direct relevance to the user of the receiver, of the noise affecting their ability to read or decode signals.

The band-by-band corrections in *wsprdaemon* can also be used, in principle, to refer the noise to free space, that is, as an electric field intensity at the antenna expressed as dBμV/m. This is important when the aim is to characterize the local noise environment external to the distribution system and receiver, and especially when making direct comparisons of absolute noise levels between different locations. However, it is not straightforward to obtain the antenna factor, ground wave gain and equivalent monopole antenna noise factor that are required to determine the field strength as described in ITU-R P.372-13 **[18]**. This is because the relative antenna factor and ground characteristics, as well as polarization and wave arrival angle contributions, may not be well known for a given comparative installation.

Even these initial steps for us as amateurs, of estimating noise at a number of locations in different countries and making the data available to all in real time has attracted the attention of professional ionospheric scientists within the HamSci community **[19]**. They appreciate the capability of radio amateurs to gather and disseminate carefully calibrated data and they are keen to apply their knowledge to interpreting the results — for example, the reasons for the seasonal changes in noise shown in **Figure 11**. There is also the puzzle of the staggered precipitous drops in noise level at KPH and KA7OEI shown in **Figure 10**. WO7I in northern Nevada and ND7M in southern Nevada, both with KiwiSDRs, have recently installed *wsprdaemon* and started reporting noise estimates. We look forward to using their data, from north and south of a line joining KPH and KA7OEI to study further the patterns of noise variation and their origin.

Acknowledgement

We are grateful to Steve Sykes, KD2OM; Holger Gatternig, OE9GHV; and Clint Turner, KA7OEI; for permission to use their noise level data, and to Larry Hill, N2AJX, for running a series of antenna experiments for us, and to the Lowell GIRO Data Center (LGDC) for Millstone Hill ionograms for 9 November 2019. We are also grateful to the Maritime Radio Historical Society for their support, permission to host a bank of KiwiSDRs, and to the Point Reyes National Seashore, National Park Service for access to the KPH antennas.

Gwyn Griffiths, G3ZIL, was first licensed in 1970 as GW3ZIL. He spent his career developing instruments for marine scientists, becoming UK National Oceanography Center's Chief Technologist and Professor of Underwater Systems at Southampton University. Since retiring in 2012 he has returned to amateur radio, concentrating on using WSPR and data analysis to understand HF band noise and minimize its impact on reception.

Rob Robinett, AI6VN, is CEO and Founder of Mystic Video, a Silicon Valley developer of professional TV broadcasting products. After a 40-year hiatus he resumed his interest in amateur radio in 2017 with a particular interest in optimizing RF receiving systems. He has deployed SDR and WSPR receive systems at the historic KPH receive site and a second set at a rural location on Maui.

Glenn Elmore, N6GN, was first licensed in 1961 as WV6STS. He has been active in RF-microwave pursuits as a career and as his radio hobby since then. He has discovered, made advances in the theory and application and published papers on, surface wave transmission lines. He has been actively involved in applying WSPR to VHF/UHF measurements and lately in pursuing the limits of small broadband antenna systems in the LF-HF region as part of the KiwiSDR project.

Notes

[1]See **rsgb.org/main/technical/propagation/noise-floor-study/hf-noise-monitoring-campaign/**.

[2]See **hf.r-e-f.org/c4_iaru_r1/16_Vienne/VIE16_C4_15_VERON_Provisional%20Results%20of%20Measurement%20Campaign.pdf**.

[3]See **rfnoise.amsatsa.org.za/about_us.php**.

[4]See **vienna.iaru-r1.org/wp-content/uploads/2019/01/VIE19-C7-002-DARC-ENAMS.pdf**.

[5]Available at **www.researchgate.net/publication/283088496_HF_radio_noise_emissions_measured_at_Key_West_Florida_March_-_October_2010**.

[6]See **www.radiomarine.org/**.

[7]The source code for the *wsprdaemon* program that includes our noise analysis methods is available online at **github.com/rrobinett/wsprdaemon**.

[8]Data can be selected, plotted and downloaded from **logs.wsprdaemon.org:3000** using Open for user ID and password.

[9]Available at **sox.sourceforge.net/**.

[10]Information on the KiwiSDR is available at **kiwisdr.com/** and on **kiwirecorder.py** at **github.com/jks-prv/kiwiclient**.

[11]A detailed technical report on the method development and calibration is available at **www.researchgate.net/publication/334612025_Estimating_LF-HF_band_noise_while_acquiring_WSPR_spots**.

[12]G. Lott, W. Stark, and M. Bail. "Multi-location long-term HF noise measurements and comparison to ITU-R P. 372-8," *Proceedings 10th IET International Conference on Ionospheric Radio Systems and Techniques (IRST 2006)*, 2006 pp. 133–137.

[13]See **arrl-ohio.org/SEC/nvis/Modified%20AS-2259%20NVIS%20Antenna.pdf**.

[14]The ionograms are available at **lgdc.uml.edu/common/DIDBDayStationStatistic?ursiCode=MHJ45&year=2019&month=11&day=9**. Further information on the Global Ionospheric Radio Observatory can be found in B. W. Reinisch and I. A. Galkin, "Global ionospheric radio observatory (GIRO)," *Earth, Planets, and Space*, 63, (2011) pp. 377-381, **https://link.springer.com/article/10.5047/eps.2011.03.001**.

[15]Daily plots of FFT and RMS noise estimators from 2200 m to 10 m for a number of reporters are available at **wsprdaemon.org** and are likely to show a range of differences between the two noise estimators.

[16]The daytime noise plateau is not always present at KA7OEI, interested readers can explore this and other wsprdaemon noise data sets using the Grafana tool, the KA7OEI 80 m data is at Note [8].

[17]Use the calculator at **www.esrl.noaa.gov/gmd/grad/solcalc/**.

[18]Available at **www.itu.int/rec/R-REC-P.372-14-201908-I/en**.

[19]See **hamsci.org/**.

Technical Notes

More on Extending the Matching Range of an 80 m Antenna

I really enjoyed the article by Bob DePierre, K8KI, titled "Extend the Matching Range of Your 80 m Antenna" in the May/June 2020 *QEX*. The issue of 80 m antennas not covering the entire band is an old one, and he offers a relatively simple solution to cover most of the band. His discussion of capacitors to handle the required power level is also very relevant.

His Appendix 1 shows how to create your own *s1p* file from MFJ-259 data to import into AE6TY's *SimSmith* program. An issue here is that the MFJ-259 does not tell you the sign of the reactance — it could be positive (inductive) or negative (capacitive). The following is a possible way to figure this out — but I'm not sure the logic is 100% true every time.

When sweeping your antenna, carefully note if the reactance goes through zero. If the reactance doesn't go through zero, then that tells you the reactance is always inductive or always capacitive. My **Figure A** shows both of these scenarios using the impedance values in Figure 6 of the K8KI article — his are truly all inductive as I believe he had already measured the impedances with a Rig Expert AA series analyzer, which does give the sign. The solid line is for reactance values that are all inductive, and the dashed line is for reactance values that are all capacitive. Which one is it? In general, as the frequency increases, the reactance goes more positive. [Impedance curve values rotate clockwise on the Smith chart when frequency increases. This suggests that the solid (top) curve is the correct one. — *Ed.*]. Thus the top curve is a good assumption. If you implement your solution with that assumption, and the measured results follow the Smith chart results, then you've guessed correctly!

If the reactance does go through zero — crosses the real axis of the Smith chart, the data in Figure 6 could be doing that if you didn't pay attention to the reactance as you were sweeping your antenna — you still have the sign issue. Again, in general, as the frequency increases, the reactance goes more positive. My **Figure B** shows this if the reactance went to zero between 3.6 MHz and 3.7 MHz, and we use the "higher inductive reactance as the frequency increases" generality. But I'm somewhat leery of this result, as the lengths between frequencies on the Smith chart should normally be decreasing as the frequency increases.

To reiterate, this logic to resolve the sign of the reactance may not work 100% of the time. And it applies only to measurements at the antenna — not at the end of a run of coax (this makes matters more difficult). If there are more elaborate ways to resolve the sign issue with an MFJ-259, I'd love to hear about them. — *Best regards, Carl Luetzelschwab K9LA,* ***k9la@arrl.net***.

450 - Ohm Window Transmission Line Fire Hazard

This note is to alert you to a dangerous condition that happened to me. Hopefully you can avoid this in your station. While in a contact on 7 MHz with friends of my radio club F6KFA, I stopped transmitting after noticing a fluctuating SWR. I started testing after lunch, but the problem persisted. My 450-Ω window line is 50 meters long, and is made up of several sections joined by soldering.

After inspecting the sections that crossed my basement, I went out to the garden to inspect the rest of the line and was stunned! My window transmission line was being consumed by fire! It was well on the way to burning entirely toward the antenna (**Figure C**). Of course, I immediately stopped the

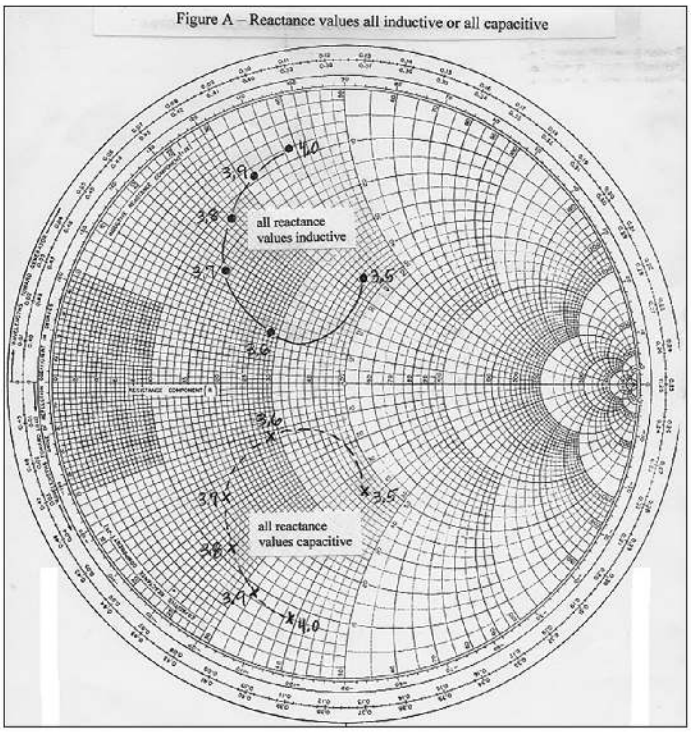

Figure A — The upper solid trace assumes positive values of reactances, the bottom dashed trace assumes negative reactance values for the impedance values in Figure 6 of the K8KI article.

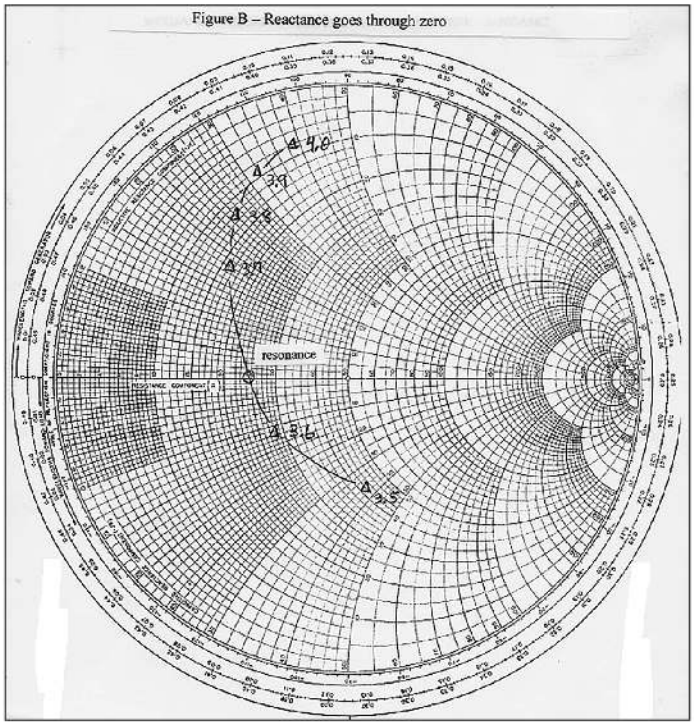

Figure B — As the frequency increases, the reactance becomes more positive.

combustion by blowing out the two small flames that were progressing quite nicely.

The fire occurred 20 meters from the antenna, a Levy 2x20m, therefore it was at a peak of the standing wave voltage at 7 MHz — just at the location of a solder joint between two sections. I had taped over the solder connections using insulating black electrical tape (of questionable quality). I did not tape over each conductor separately but instead I taped around both conductors of the whole line. This exposed the solder joints to thousands of volts peak-to-peak maximum voltage at my transmitting power level of 500 W.

The fire occurred on the portion of transmission line in my garden. Had it happened inside the house near a wooden frame where the line crosses two door frames, this could have started a catastrophic house fire!

I recommend that you check the routing of your high impedance transmission lines, and be careful about using any added insulation on your lines! A version of this article appeared in the May 2014 issue of *Radio-REF* (Réseau des Émetteurs Français, **www.r-e-f.org**).— *73 André Champel, F5SQ;* ***champel.andre@orange.fr***.

Send your short *QEX* Technical Note to the Editor, via email to qex@arrl.org. We reserve the right to edit your Note for clarity, and to fit in the available page space. "*QEX* Technical Note" may also appear in other ARRL media. The publishers of *QEX* assume no responsibilities for statements made by correspondents.

Figure C — Burned-out insulation of the window transmission line section.

Letters

Extend the Matching Range of Your 80 m Antenna, (May/June 2020)

Dear Editor,

Concerning Appendix 2 on page 27 of the *QEX* article by Bob DePierre, what am I missing? Why is the peak-to-peak voltage calculated instead of just the peak voltage? Doesn't the capacitor just see the peak voltage with a reversal of sign every half cycle? — *Best regards, Lawrence Joy, WN8P, Copemish, MI.*

The author responds

Thanks for your questions, Larry. Calculating the voltage across a component at some instant in time versus determining a component specification requires different methodologies. For the case in my article, my concern was to specify a conservative value that was going to be safe. I specified the required breakdown voltage of a component with an abundance of caution — in this case calculating the peak-to-peak voltage across the capacitor at twice the stress value — that would be a conservative procedure. Use my procedure, and your equipment will not be damaged by a under-specified component. — *73, Bob DePierre, K8KI, Huntsville, AL.*

The Versatile Double Balanced Mixer — Part 2. (July/August 2020)

Dear Editor,

Eric Nichols, KL7AJ, included pages from the *Bell System Technical Journal* in his QEX article. The *BSTJ* archives are available online at **https://onlinebooks.library.upenn.edu/webbin/serial?id=belltechj.** — *73, Jon Titus, KZ1G, Herriman, UT.*

Send your *QEX* Letters to the Editor to, ARRL, 225 Main St., Newington, CT 06111, or by fax at 860-594-0259, or via email to qex@arrl.org. We reserve the right to edit your letter for clarity, and to fit in the available page space. "Letters to the Editor" may also appear in other ARRL media. The publishers of *QEX* assume no responsibilities for statements made by correspondents.

Upcoming Conferences

ARRL and TAPR Digital Communications Conference

September 11 – 12, 2020

www.tapr.org/2020-arrl-tapr-dcc-update

The 39th Annual ARRL and TAPR Digital Communications Conference (DCC) will be a virtual conference on September 11 and 12, using Zoom video communications and YouTube video-sharing platforms.

Registered DCC attendees participating via Zoom will be able to interact with presenters and other attendees via a chat room as well as raise a virtual hand to ask questions. Ad hoc "lightning talks" on various topics of interest will be announced throughout the DCC. Hardware and software demonstrations will be conducted during the DCC by means of Zoom's breakout room feature. See website for registration information (you don't need a Zoom account to register).

Non-registered DCC attendees can watch the live stream for free on YouTube, however, non-registered DCC attendees will not be able to ask questions or chat. No registration is required for YouTube access (the YouTube URL will be announced and posted to the website preceding the DCC).

DCC registration is free for TAPR members and $30 for non-members. Members receive a 100% discount at checkout. Non-members who would like to join TAPR and receive the free DCC pass can simply add TAPR membership and DCC registration to their shopping carts. After checkout, they will receive the free DCC pass when their membership is processed.

Conference papers will be distributed as PDFs to participants. Printed copies of the papers will be available for sale at **www.lulu.com**.

GNU Radio Conference — Virtual GRCon20

September 14 – 18, 2020

www.gnuradio.org/grcon/grcon20

GRCon20 will be held September 14, 2020 online as a virtual event. The organizing team is hard at work creating a fun and interactive experience.

GNU Radio Conference (GRCon) is the annual conference for the GNU Radio project and community, and has established itself as one of the premier industry events for Software Radio. It is a week-long conference that includes high-quality technical content and valuable networking opportunities. GRCon is a venue that highlights design, implementation, and theory that has been practically applied in a useful way. GRCon attendees come from a large variety of backgrounds, including industry, academia, government, and hobbyists.

See website for more details, including registration.

Microwave Update 2020

October 15 – 18, 2020
POSTPONED to 2021
Sterling, Virginia

www.microwaveupdate.org
www.ntms.org

Microwave Update 2020, sponsored by the North Texas Microwave Society, has been postponed to 2021. Information will be added to the website as it becomes available.

38th Annual AMSAT Space Symposium and Annual General Meeting

October 16 – 18, 2020

[Virtual Event being planned; in-person postponed]

Bloomington, Minnesota

www.amsat.org

The 38th Annual AMSAT Space Symposium and Annual General Meeting in-person event scheduled to be held in Bloomington, Minnesota has been canceled. The event will be shifted to a virtual, online platform. This comes after a decision made between AMSAT's Senior Leadership and Board of Directors in response to the ongoing COVID-19 pandemic. While AMSAT recognizes the national challenges related to recent events in Minneapolis, they have no bearing on the Symposium decision whatsoever. We anticipate holding 2021's Annual Space Symposium at the previously announced 2020 venue in Bloomington, Minnesota.

The in-person event was scheduled to occur Friday, October 16th – Sunday, October 18th. As the 2020 virtual event plans are developed, they will be announced via the usual AMSAT channels.

Build Your Go-Kit with DX Engineering!

Coaxial Cable Assemblies

These low-loss cable assemblies are available in standard lengths with DX Engineering's revolutionary patented PL-259 connector. Use the online Custom Cable Builder at DXEngineering.com to build assemblies made to your exact specs. DX Engineering's coaxial cable is also available by the foot or in bulk spools.

Equipment Cases

Protect your sensitive equipment! DX Engineering boasts three rugged options to keep your gear safe: virtually indestructible Gator Equipment Rack Cases for transporting everything you need in your Go-Kit; high-impact resin NANUK cases, including units that perfectly fit RigExpert Antenna Analyzers; and iPortable units that combine a travel case with a DC power distribution point, speaker, and rack shelving. **Enter "Equipment Case" at DXEngineering.com.**

DC Outlet Panels and Battery Backup Systems

Bid farewell to that annoying tangle of spaghetti wire with RIGrunner DC outlet panels from West Mountain Radio. These outlets are fused for protection and ensure you have reliable power distribution. They provide 40 amps of maximum power and include from 4 to 12 Powerpole® connectors. West Mountain also makes backup devices, such as the Super PWRgate, which instantly switches to battery backup if you lose power. **Enter "West Mountain" at DXEngineering.com.**

Power Supplies

Make DX Engineering your source for reliable switching and linear power supplies from major brands, including Alinco, Ameritron, Astron, Kenwood, Yaesu, and more. Choose from units with input voltages from 85 to 260 Vac and peak outputs from 10 to 50 amps. **Enter "Power Supplies" at DXEngineering.com.**

Antenna Tuners

DX Engineering carries a great lineup of LDG Electronics innovative automatic tuners to match just about any antenna and maximum power handling requirement, from 100 to 1,000 watts. Select from the 100W IT-100 model, which is ideal for Icom rigs; the 100W YT-100, designed for specific Yaesu radios; the QRP-friendly Z-817 auto-tuner; the Z-100Plus, featuring 2,000 memories that store both frequency and tuning parameters; and many more. **Enter "LDG Tuner" at DXEngineering.com.**

Wire Antennas

Need a portable wire antenna? You'll find it here! Models include DX Engineering's versatile EZ-BUILD UWA Center T and End Insulator Kits that let you build virtually any wire antenna type; fan dipoles from EAntenna that use multiple parallel wires with spacers to allow each band dipole to remain separate; SOTABeams' portable and pre-assembled wire antenna kits, including its Band Hopper 3- and 4-band dipoles; and an impressive selection from Alpha Delta, Buckmaster, Bushcomm, and others. **Enter "Wire Antenna" at DXEngineering.com.**

Tigertronics SignaLink™ USB Digital Communication Interface Packages

These combos pair a Tigertronics SignaLink USB with radio-specific interface cables for Alinco, Elecraft, Icom, Kenwood, Yaesu, and other rigs. Made for simple hookup to a Mac or PC, the SignaLink USB comes with a built-in low-noise sound card that supports all digital and voice modes, including WSJT. **Enter "Tigertronics" at DXEngineering.com.**

DX Engineering's Amateur Radio Blog for New and Experienced Hams.
Visit OnAllBands.com for information you can use to improve your on-air experience.

Free Standard Shipping for Orders Over $99. If your order, before tax, is over 99 bucks, then you won't spend a dime on ground shipping. (Additional special handling fees may be incurred for Hazardous Materials, Truck Freight, International Orders, Next Day Air, Oversize Shipments, etc.).

Showroom Staffing Hours:
9 am to 5 pm ET, Monday-Saturday

Ordering (via phone):
8:30 am to midnight ET, Monday-Friday
9 am to 5 pm ET, Weekends

Phone or e-mail Tech Support: 330-572-3200
8:30 am to 7 pm ET, Monday-Friday
9 am to 5 pm ET, Saturday
All Times Eastern I Country Code: +1
DXEngineering@DXEngineering.com

800-777-0703 | DXEngineering.com

CELEBRATING 20 YEARS 2000-20

We're All Elmers Here! Ask us at: Elmer@DXEngineering.com
Email Support 24/7/365 at DXEngineering@DXEngineering.com

GET OUT OF THE GREY
AND INTO THE GREEN

SteppIR Antenna Systems are designed for performance, period. We offer Yagi, vertical and dipole antennas in configurations designed to satisfy requirements at every level. Our antennas mechanically adjust utilizing stepper motors, so that the antenna is the exact physical length required at EVERY frequency within its range. Fixed length aluminum antenna manufacturers use traps, interlacing or simply add more elements to "trick" the radio into thinking it is resonant – but there is no substitute for having a resonant, optimized antenna.

It doesn't matter if you are just starting out in amateur radio, are an expert operator or belong somewhere in between... Step up to SteppIR and experience the thrill of "working them on the first call"!

YAGI ANTENNAS
The best performing and only truly optimized HF antennas available

VERTICAL ANTENNAS
True quarter wave continuous coverage

PORTABLE ANTENNAS
Full legal limit power handling capability for large DXpeditions or the family vacation

ANALYZERS
Test on the fly with our range of handheld antenna analyzers

EMERGENCY COMMUNICATIONS
In disaster situations, there is no room for compromise

steppIR
COMMUNICATION SYSTEMS

FOR DETAILS, SPECS AND TO ORDER:

www.steppir.com 425-453-1910